

Robust numerical methods for taxis–diffusion–reaction systems: Applications to biomedical problems

A. Gerisch^{a,*}, M.A.J. Chaplain^b

^a *Institut für Numerische Mathematik, Fachbereich Mathematik und Informatik, Martin-Luther-Universität Halle-Wittenberg, Postfach, 06099 Halle (Saale), Germany*

^b *Department of Mathematics, University of Dundee, Dundee, DD1 4HN, Scotland, UK*

Received 21 May 2004; accepted 21 May 2004

Abstract

In this paper we consider the numerical solution of taxis–diffusion–reaction models. Such nonlinear partial differential equation models appear often in mathematical biology and we consider examples from tumour growth and invasion, and the aggregation of amoebae. These examples are characterised by a taxis term which is large in magnitude compared with the diffusion term and this can cause numerical problems. The numerical technique presented here follows the method of lines. Special attention is paid to the discretization of the taxis term in space to avoid oscillations and negative solution values. We employ splitting techniques in the time discretization to deal with the complex structure of the model and to reduce the amount of computational linear algebra. These techniques are based on explicit Runge–Kutta and linearly implicit Runge–Kutta–Rosenbrock methods. A series of numerical experiments demonstrates the good performance of the algorithm and gives rise to some implications for future modelling.

© 2005 Elsevier Ltd. All rights reserved.

Keywords: Taxis; Diffusion–reaction; Numerical solution; Method of lines; Splitting methods

1. Introduction

Many biological systems exhibit time dependent reaction–diffusion phenomena on an open, bounded domain $\Omega \subset \mathbb{R}^d$ (in this work we consider $d = 1$ or $d = 2$, and the numerical methods are presented for $d = 2$; however, they are applicable for all $d \geq 1$) with a piecewise smooth boundary $\partial\Omega$. These phenomena generally involve several interacting chemical species (e.g. propagator species, controller variables, inhibitors, enhancers, attractors). We denote the time and space dependent concentrations of the chemical species by the vector valued function

$$\mathbf{c} : [0, T] \times \bar{\Omega} \rightarrow \mathbb{R}^l.$$

The processes occurring in such systems involve kinetic interactions between the various chemical species as well as the spatial spread of the chemicals and so are often modelled by systems of partial differential equations (PDEs) of

* Corresponding author.

E-mail addresses: gerisch@mathematik.uni-halle.de (A. Gerisch), chaplain@maths.dundee.ac.uk (M.A.J. Chaplain).

reaction–diffusion type. The generic reaction–diffusion system may be written as

$$\partial_t \mathbf{c}(t, \mathbf{x}) = \mathbf{D} \Delta \mathbf{c}(t, \mathbf{x}) + \mathbf{g}(\mathbf{c}(t, \mathbf{x})) \quad \text{for } (t, \mathbf{x}) \in (0, T] \times \Omega, \quad (1)$$

where $\partial_t = \frac{\partial}{\partial t}$, the Laplacian Δ operates componentwise on \mathbf{c} , \mathbf{D} is an l -by- l nonnegative diagonal matrix containing the diffusion coefficient of each species and the function $\mathbf{g} : \mathbb{R}^l \rightarrow \mathbb{R}^l$ describes the reaction kinetic between the species. We permit certain of the diffusion coefficients to be zero (which may model, for example, chemicals bound to an underlying substratum or extracellular matrix). The system also has to be supplied with appropriate initial and boundary conditions.

If the domain Ω , beside the chemicals \mathbf{c} , also contains any entities or organisms (e.g. cells, predators, parasitoids) which migrate in direct response to the concentration fields of some of the chemicals in \mathbf{c} , then this migration process will clearly depend on the dynamics of the underlying reaction–diffusion system for \mathbf{c} . We denote the density of the organisms by the function

$$n : [0, T] \times \bar{\Omega} \rightarrow \mathbb{R}.$$

If the migration depends on the concentration field of a soluble (diffusible) chemical then the process is termed *chemotaxis*; if this chemical is bound to some underlying substratum (e.g. extracellular matrix) then we talk about *haptotaxis* (other forms of taxis are also possible, e.g. galvanotaxis, phototaxis, gravitaxis [1]). A chemical may have either an attracting or a repelling influence on the migration of the organisms depending on the interactions between them. In both cases, the migration due to taxis is assumed to be proportional to the gradient (in space) of the chemical. Further, there might be some random motility of the organisms, and death or birth might also occur (potentially depending on \mathbf{c}). The generic equation describing the evolution of $n(t, \mathbf{x})$ is then given by

$$\partial_t n = \varepsilon \Delta n - \nabla \cdot \left(n \sum_{j=1}^l p_j(\mathbf{c}) \nabla c_j \right) + f_0(n, \mathbf{c}) \quad \text{for } (t, \mathbf{x}) \in (0, T] \times \Omega, \quad (2)$$

where ε is the random motility coefficient (cf. chemical diffusion) and the taxis functions associated with each chemical c_j , denoted by $p_j : \mathbb{R}^l \rightarrow \mathbb{R}$, $j = 1, \dots, l$, as well as the reaction term $f_0 : \mathbb{R} \times \mathbb{R}^l \rightarrow \mathbb{R}$ are given. The gradient operator is denoted by ∇ .

In biological systems where the organisms directly interact with the chemical species, the density $n(t, \mathbf{x})$ also has an influence on the dynamics of the underlying reaction–diffusion system, for instance through the production or uptake of certain of the chemicals. Therefore the quantity n should be included in the reaction term \mathbf{g} of Eq. (1) such that we now have a function $\mathbf{g}_0(n, \mathbf{c})$. Altogether we obtain the taxis–diffusion–reaction (TDR) system

$$\partial_t n = \varepsilon \Delta n - \nabla \cdot \left(n \sum_{j=1}^l p_j(\mathbf{c}) \nabla c_j \right) + f_0(n, \mathbf{c}), \quad (t, \mathbf{x}) \in (0, T] \times \Omega. \quad (3a)$$

$$\partial_t \mathbf{c} = \mathbf{D} \Delta \mathbf{c} + \mathbf{g}_0(n, \mathbf{c}), \quad (3b)$$

Again, this system has to be supplied with appropriate initial and boundary conditions.

A simple example of a TDR system in one space dimension is the model of Chaplain and Stuart [2] describing the response of endothelial cells (n) to a chemoattractant chemical (c_1) during the process of tumour-induced angiogenesis. The equations are given by

$$\begin{aligned} \partial_t n &= \varepsilon \partial_x^2 n - \partial_x (n \chi_0 \partial_x c_1) + \max\{0, c_1 - c_1^*\} \mu n (1 - n) - \beta n, \\ \partial_t c_1 &= D \partial_x^2 c_1 - \frac{\alpha n c_1}{\gamma + c_1} - \lambda c_1, \end{aligned}$$

where we use the notation $\partial_x = \frac{\partial}{\partial x}$.

In this paper we will focus on biological systems where the movement (or migration) of organisms is mainly due to taxis with little due to random motion, or where there is no random motility at all. We therefore consider the case $\varepsilon = 0$ in all these systems and study the effects of this change to the models.

In particular we are concerned in this paper with developing robust numerical methods to solve such systems as (3) with $\varepsilon = 0$ on the unit interval $\Omega = (0, 1)$ and the unit square $\Omega = (0, 1)^2$. We note that we can add a further time

and space dependent function (e.g. $h(t, \mathbf{x})$) to each of the equations accounting for any sources and sinks. This can be useful if the models considered here are going to be coupled with other models.

The paper is organised as follows. Section 2 contains a description of certain specific biomathematical models which we will use to test our numerical techniques on. Next, in Section 3 we give details of the numerical techniques which are used for the solution of the model equations. Simulation results for the models from Section 2 are then reported in Section 4. Finally, in Section 5, we discuss the biological implications of zero random motility of the organisms and comment on the appropriateness of numerical schemes. We also give implications for future modelling.

2. TDR models

In this section we describe several mathematical models which are of the general form given in (3). The first model is actually not really a TDR system but a scalar taxis equation. We give an analytic solution for this problem. The availability of this solution makes this model ideal for testing our numerical schemes. The next three models arise from the study of certain aspects of tumour growth (angiogenesis and invasion) and the fifth and final example is taken from developmental biology, specifically the study of the aggregation phase of the social amoeba *Dictyostelium discoideum*. Other TDR models arise, for instance, from modelling fungal growth and interaction [3] and fracture healing in bone [4].

2.1. A simple taxis test model

This model is taken from [5] and we use it to evaluate our taxis discretization algorithm. The spatial domain of the model is the unit square, $\Omega = (0, 1)^2$. In the model, a scalar quantity (density n) is simply advected up the gradient of an attractant with fixed concentration profile. The attractant concentration is radially symmetric with centre $(1/2, 1/2)$:

$$c_1(t, \mathbf{x}) := \tilde{c}(r(\mathbf{x})) = 1 - \cos(4\pi r(\mathbf{x})) \quad \text{for all } (t, \mathbf{x}) \in [0, T] \times \bar{\Omega},$$

where $r(\mathbf{x}) := ((x_1 - 1/2)^2 + (x_2 - 1/2)^2)^{1/2}$, is the distance of \mathbf{x} from the centre of Ω . This corresponds to a ring of chemoattractant with maximum at $r = 0.25$. The model equation is given by

$$\partial_t n = -\nabla \cdot (n \nabla c_1), \quad \text{for } (t, \mathbf{x}) \in (0, T] \times \Omega. \tag{4}$$

We use parametrised initial data with parameter $0 \leq \varepsilon < 0.1$:

$$n(0, \mathbf{x}) = n_\varepsilon(r(\mathbf{x})) = \begin{cases} 1 & : r \leq 0.4 - \varepsilon \\ \frac{1}{2} \left(1 + \cos \left(\frac{r - 0.4 + \varepsilon}{2\varepsilon} \pi \right) \right) & : |r - 0.4| < \varepsilon \\ 0 & : r \geq 0.4 + \varepsilon. \end{cases} \tag{5}$$

These initial data have continuous first derivatives in space if $\varepsilon > 0$. The parameter ε controls the steepness of the front in the initial data. We use two different values in our experiments: $\varepsilon = 0.09$ for a fairly smooth initial condition, and $\varepsilon = 0$ which is a jump initial condition with jump at $r = 0.4$. The initial condition and its gradient are zero for all $r \geq \frac{1}{2}$ if $\varepsilon < 0.1$. We assume no flux boundary conditions for n . This is consistent with the initial data, and, together with the given attractant concentration, implies that the boundary has no influence on the solution in Ω . As time proceeds, the population n moves up the gradient of c_1 and tends to cluster into a ridge at $r = 0.25$ where c_1 has its maximum value.

The solution n of this problem is radially symmetric and we define $\tilde{n}(t, r)$ such that $n(t, \mathbf{x}) = \tilde{n}(t, r(\mathbf{x}))$ for all $\mathbf{x} \in \bar{\Omega}$. Further define $v(r) := \tilde{c}'(r) = 4\pi \sin(4\pi r)$. Then we obtain (see also [5])

$$\begin{aligned} \nabla \cdot (n \nabla c_1) &= \nabla \cdot (\tilde{n} v \nabla r) \\ &= (v \partial_r \tilde{n} + \tilde{n} v') \nabla r \cdot \nabla r + \tilde{n} v \Delta r \\ &= v \partial_r \tilde{n} + \tilde{n} v' + \tilde{n} v r^{-1} \end{aligned}$$

and hence Eq. (4) is for $r > 0$ equivalent to $\partial_t \tilde{n} + v \partial_r \tilde{n} = -(v' + v r^{-1}) \tilde{n}$. This equation can be solved by the method of characteristics (we can restrict our attention to $r \in [0, 1/2]$) and we obtain for smooth initial data $\tilde{n}(0, r) := \tilde{n}_0(r)$

and $r \neq 0, 1/4, 1/2$

$$\tilde{n}(t, r) = \tilde{n}_0(s(t, r)) \frac{s(t, r) \sin(4\pi s(t, r))}{r \sin(4\pi r)}, \quad (6)$$

with

$$s(t, r) = \frac{1}{2\pi} \arctan\left(\frac{\tan(2\pi r)}{\exp(16\pi^2 t)}\right) + \frac{\text{int}(4r) + (\text{int}(4r) \bmod 2)}{4},$$

where $\text{int}(z)$ is the integer part of $z \in \mathbb{R}$, $z \geq 0$. We obtain the solution for $r = 0, 1/4, 1/2$ by continuity. Hence we have a smooth (classical) solution for all $t > 0$ whenever the initial data are differentiable. If the initial data are nondifferentiable at some points then Eq. (6) can still be evaluated and is a generalised solution; see e.g. [6, p. 21]. For a detailed derivation of the solution we refer the interested reader to [7].

2.2. Mathematical modelling of tumour growth and invasion

The development of a primary solid tumour (e.g., a carcinoma) begins with a single normal cell becoming transformed as a result of mutations in certain key genes. This transformed cell differs from a normal one in several ways, one of the most notable being its escape from the body's homeostatic mechanisms, leading to inappropriate proliferation. An individual tumour cell has the potential, over successive divisions, to develop into a cluster (or nodule) of tumour cells. Further growth and proliferation leads to the development of an avascular tumour consisting of approximately 10^6 cells. This cannot grow any further, owing to its dependence on diffusion as the only means of receiving nutrients and removing waste products. For any further development to occur the tumour must initiate angiogenesis — the recruitment of blood vessels. The tumour cells first secrete angiogenic factors which in turn induce endothelial cells in a neighbouring blood vessel to degrade their basal lamina and begin to migrate towards the tumour. As it migrates, the endothelium begins to form sprouts which can then form loops and branches through which blood circulates. From these branches more sprouts form and the whole process repeats, forming a capillary network which eventually connects with the tumour, completing angiogenesis and supplying the tumour with the nutrients it needs to grow further. During the process of vessel formation, the endothelial cells may secrete enzymes which degrade the local tissue (extracellular matrix) thus facilitating the whole process. Indeed this process of matrix degradation through enzyme secretion is also carried out by the tumour cells themselves. This enables active migration by the tumour cells into the tissue to take place. The combination of tumour vascularisation (i.e. the blood vessels connect with the tumour) and active tissue invasion means that there is now the possibility of tumour cells finding their way into the circulation and/or lymph system, and subsequently being deposited in distant sites in the body, resulting in metastasis.

The complete process of metastasis involves several sequential steps, each of which must be successfully completed by cells of the primary tumour before a secondary tumour (a metastasis) is formed. A summary of the key stages of the metastatic cascade is as follows:

1. the primary tumour induces the formation of a local vascular network and creates its own blood supply;
2. cancer cells escape from the primary tumour;
3. the cells locally degrade the surrounding tissue and continue migration;
4. they enter the lymphatic and blood circulation systems (*intravasation*);
5. they must survive their journey in the circulation system;
6. they must escape from the blood circulation (*extravasation*);
7. the cancer cells (from the primary tumour) must then establish a new colony in distant organs;
8. the new colony of cells must then begin to grow to form a secondary tumour in the new organ.

The mathematical models which we will present in the following two sections focus specifically on the processes of tumour-induced angiogenesis (endothelial cell migration in response to external stimuli, i.e. point 1) and tumour invasion of tissue (cancer cell migration, i.e. points 2 and 3).

2.2.1. Mathematical models of tumour-induced angiogenesis

Angiogenesis, the formation of blood vessels from a pre-existing vasculature, is a crucial component of many mammalian growth processes, including embryogenesis and wound healing. It is also a key component in the metastatic cascade enabling a solid tumour to progress from the relatively harmless avascular growth phase to the potentially lethal vascular growth phase. The mathematical modelling of angiogenesis may be traced back to the work of D’Arcy Thompson (1917) [8]. In more recent times a variety of models have appeared focusing on different aspects of the process [9,2,10–14], while the recent work of Valenciano and Chaplain [15,16] has focussed not only on the modelling aspects of tumour-induced angiogenesis but also on developing efficient numerical techniques using finite element methods. A comprehensive account of the complete angiogenic process may be found in [11] and references therein. We summarise the main events of angiogenesis as:

- the secretion of chemicals known as tumour angiogenic factors (TAF) by cancer cells,
- the response of endothelial cells (EC) in any neighbouring blood vessels to these chemicals through migration and proliferation,
- interaction between the endothelial cells and the extracellular matrix,
- the formation of new individual capillary sprouts, which in turn connect up to form a new vasculature,
- flow of blood and remodelling of the vasculature.

We describe below two models of tumour-induced angiogenesis developed by Chaplain and Stuart [2] and Anderson and Chaplain [11].

Model 1:

The model of Chaplain and Stuart [2] focused on two key variables, namely the EC density (n) and TAF concentration (c_1). The model assumed that TAF was secreted by tumour cells (located on one boundary of the domain), diffused into the surrounding tissue, was taken up by the endothelial cells via cell-surface receptors and underwent some natural decay. The motion of the endothelial cells was assumed to be influenced by two factors only: random motility (analogous to molecular diffusion) and chemotaxis in response to TAF gradients. To derive the partial differential equation governing endothelial cell motion, the total cell flux was considered and then a conservation equation was derived for the cell density. The contributions to the endothelial cell flux \mathbf{J}_n were given by

$$\mathbf{J}_n = \mathbf{J}_{\text{random}} + \mathbf{J}_{\text{chemo}}.$$

To describe the random motility of the endothelial cells a flux of the form $\mathbf{J}_{\text{random}} = -\varepsilon \nabla n$, where ε is a positive constant, the cell random motility coefficient, was assumed. The chemotactic flux was taken to be of the simple form $\mathbf{J}_{\text{chemo}} = \chi_0 n \nabla c_1$, where χ_0 is the (constant) chemotactic function. The endothelial cells were also assumed to undergo death at rate β and proliferation in a logistic manner, with proliferation constant μ . The latter was assumed to be governed by a threshold TAF concentration c_1^* , i.e. there was no proliferation for $c_1 < c_1^*$ and logistic proliferation for $c_1 > c_1^*$. The nondimensionalised model equations are then given by

$$\begin{aligned} \partial_t n &= \overbrace{\varepsilon \Delta n}^{\text{random motility}} - \overbrace{\nabla \cdot (\chi_0 n \nabla c_1)}^{\text{chemotaxis}} + \overbrace{\max\{0, c_1 - c_1^*\} \mu n (1 - n)}^{\text{proliferation}} - \overbrace{\beta n}^{\text{cell death}} \\ \partial_t c_1 &= \overbrace{\Delta c_1}^{\text{diffusion}} - \overbrace{\frac{\alpha n c_1}{\gamma + c_1}}^{\text{uptake by cells}} - \overbrace{\lambda c_1}^{\text{decay}}. \end{aligned} \tag{7}$$

Chaplain and Stuart estimated the model parameters from experimental data and they are as follows:

$$\varepsilon = 0.001, \quad \alpha = 10, \quad \gamma = 1, \quad \lambda = 1, \quad \chi_0 = 0.75, \quad \mu = 100, \quad \beta = 4, \quad c_1^* = 0.2.$$

The above parameter estimation shows that the cell random motility is much smaller than the chemotaxis. Hence, in addition, in Section 4 we also consider the system without cell random motility:

$$\begin{aligned} \partial_t n &= -\nabla \cdot (\chi_0 n \nabla c_1) + \max\{0, c_1 - c_1^*\} \mu n (1 - n) - \beta n \\ \partial_t c_1 &= \Delta c_1 - \frac{\alpha n c_1}{\gamma + c_1} - \lambda c_1. \end{aligned} \tag{8}$$

We consider the systems (7) and (8) in Section 4.2 on the domain $\Omega = (0, 1)$ and give a set of suitable initial and boundary conditions there.

Model 2:

The model of Anderson and Chaplain [11] extended and further developed the model of Chaplain and Stuart [2] by including the interactions between the endothelial cells and the extracellular matrix through the matrix macromolecule fibronectin. The model therefore consists of three equations governing the evolution of the three variables, EC density n , TAF concentration c_1 and fibronectin concentration c_2 .

Once again the model assumed that the motion of the endothelial cells (at or near a capillary sprout-tip) is influenced by random motility and chemotaxis (in response to TAF gradients), but also by haptotaxis in response to fibronectin gradients [17]. Once again to derive the partial differential equation governing endothelial cell motion, the total cell flux was considered and then a conservation equation was derived for the cell density. The three contributions to the endothelial cell flux \mathbf{J}_n were taken to be

$$\mathbf{J}_n = \mathbf{J}_{\text{random}} + \mathbf{J}_{\text{chemo}} + \mathbf{J}_{\text{hapto}}.$$

Once again, to describe the random motility of the endothelial cells at or near the sprout-tips, a flux of the form $\mathbf{J}_{\text{random}} = -\varepsilon \nabla n$, where ε is a positive constant, the cell random motility coefficient, was chosen. However the chemotactic flux was taken to be of the form $\mathbf{J}_{\text{chemo}} = \chi(c_1)n \nabla c_1$, where $\chi(c_1)$ is a chemotactic function, reflecting the saturation of TAF receptors on the cell surface. Finally the influence of fibronectin on the endothelial cells was modelled by the simple form of haptotactic flux, $\mathbf{J}_{\text{hapto}} = \rho_0 n \nabla c_2$, where $\rho_0 > 0$ is the (constant) haptotactic coefficient. The model omitted any proliferation terms for the cells since in this case attention was focused on the endothelial cells at the sprout-tips (where there is no proliferation).

The equation for fibronectin contained a degradation term (the endothelial cells degrade the fibronectin via enzymes) and production term since the endothelial cells themselves produce and secrete fibronectin which then becomes bound to the extracellular matrix and does not diffuse. Therefore the equation for fibronectin contains no diffusion term [17].

Following the results of Chaplain and Stuart [2] where it was noted that the TAF diffusion occurred on such a fast timescale as to set up a quasi-steady state concentration profile, the TAF equation contains only one term, that of uptake or binding of the TAF to the endothelial cell surface receptors. The initial quasi-steady state concentration profile is provided through the initial conditions for the TAF.

Hence the complete, nondimensionalised system of equations describing the interactions of the endothelial cells, TAF and fibronectin as modelled by Anderson and Chaplain [11] is

$$\begin{aligned} \partial_t n &= \overbrace{\varepsilon \Delta n}^{\text{random motility}} - \overbrace{\nabla \cdot \left(\frac{\chi_0 n}{1 + \alpha c_1} \nabla c_1 \right)}^{\text{chemotaxis}} - \overbrace{\nabla \cdot (\rho_0 n \nabla c_2)}^{\text{haptotaxis}}, \\ \partial_t c_1 &= - \overbrace{\eta n c_1}^{\text{uptake}}, \\ \partial_t c_2 &= \overbrace{\beta n}^{\text{production}} - \overbrace{\gamma n c_2}^{\text{degradation}}, \end{aligned} \tag{9}$$

This system is considered to hold on the unit square $\Omega = (0, 1)^2$ (representing a square of corneal tissue) with the parent vessel (e.g. limbal vessel) located along one edge and the tumour located on the opposite edge. These assumptions result in the choice of initial values for n , c_1 , and c_2 as given in Section 4.2. It was assumed that the cells, and consequently the capillary sprouts, remain within the domain of tissue under consideration and therefore no-flux boundary conditions of the form

$$\zeta \cdot (-\varepsilon \nabla n + n(\chi(c_1) \nabla c_1 + \rho_0 \nabla c_2)) = 0, \tag{10}$$

were imposed for n on the boundaries of the square, where ζ is an appropriate outward unit normal vector. No boundary conditions can be imposed on c_1 and c_2 .

Anderson and Chaplain [11] estimated as many parameter values as possible from experimental data and used the following set in their simulations:

$$\varepsilon = 0.00035, \quad \chi_0 = 0.38, \quad \rho_0 = 0.34, \quad \alpha = 0.6, \quad \beta = 0.05, \quad \gamma = 0.1, \quad \eta = 0.1.$$

Although Anderson and Chaplain [11] considered random migration of the endothelial cells, in this paper we also consider the system without this random motion. This can be justified biologically — prior to stimulation by the TAF, the endothelial cells are migratorily inert and are simply attached to one another while lining their parent vessel. Also we can see from the estimated parameter values ($\varepsilon = 0.00035$, $\chi_0 = 0.38$, $\rho_0 = 0.34$) that the (scaled) random migration coefficient of the EC is several orders of magnitude smaller than the taxis coefficients. The modified system we also study here is therefore given by

$$\begin{aligned} \partial_t n &= -\nabla \cdot \left(\frac{\chi_0 n}{1 + \alpha c_1} \nabla c_1 \right) - \nabla \cdot (\rho_0 n \nabla c_2), \\ \partial_t c_1 &= -\eta n c_1, \\ \partial_t c_2 &= \beta n - \gamma n c_2. \end{aligned} \tag{11}$$

2.2.2. Mathematical modelling of tumour invasion

As noted previously, a crucial part of the metastatic process is the ability of the cancer cells to degrade the surrounding tissue or *extracellular matrix* (ECM). This is a complex mixture of proteins and proteoglycans within and on which the normal cells of solid organs are situated. The matrix is highly dynamic, at any one time being actively secreted and degraded. A number of specific *matrix degradative enzymes* (MDEs) such as the *plasminogen activator* (PA) system and the large family of *matrix metalloproteinases* (MMPs) have been described and both the PAs and the MMPs have been repeatedly implicated in all of the key steps of tumour invasion and metastasis. A comprehensive description of the invasive process and its place in the metastatic cascade is given in [18] and references therein. In recent years there has been an increase in modelling the process of tumour invasion with a number of articles appearing on the subject (e.g. [19–21,18]). We describe below the recent model of Anderson et al. [18] who developed a mathematical model of tumour invasion based on generic solid tumour growth, which for simplicity was assumed to be in an avascular state. Whilst most tumours are asymptomatic at this state, it is still possible for cells to escape and migrate to the lymph nodes and for the more aggressive tumours to invade.

In the model three variables were considered; tumour cell density (denoted by n), ECM density (denoted by c_1) and MDE concentration (denoted by c_2). The main assumptions of the model were that the tumour cells produce MDEs which degrade the ECM locally and that ECM degradation results in the production of molecules which are actively attractive to tumour cells (e.g. fibronectin) and which then aid in directed tumour cell motility (haptotaxis).

The model considered tumour cell motion to be driven only by random motility and haptotaxis in response to adhesive and/or attractive gradients created by degradation of the matrix. In a manner similar to that of Anderson and Chaplain [11], the total cell flux was considered and then a conservation equation was derived for the cell density. The two contributions to the tumour cell flux \mathbf{J}_n were taken to be

$$\mathbf{J}_n = \mathbf{J}_{\text{random}} + \mathbf{J}_{\text{hapto}}.$$

To describe the random motility of the tumour cells a flux of the form $\mathbf{J}_{\text{random}} = -\varepsilon(c_1, c_2)\nabla n$ was assumed. Anderson et al. [18] considered $\varepsilon(c_1, c_2)$ to be a constant or a function of either the MDE or ECM concentration. Here we assume it is constant. The haptotactic flux was taken to be of the simple form $\mathbf{J}_{\text{hapto}} = \chi n \nabla c_1$, where $\chi > 0$ is the (constant) haptotactic coefficient. The model did not consider any proliferation of the tumour cells, but this could be easily incorporated.

Active MDEs were assumed to be produced by the tumour cells, diffuse throughout the tissue and undergo some form of decay (either passive or active). The ECM was assumed to have no motility and was degraded by the MDEs upon contact. No remodelling of the ECM was assumed, although once again, this could be easily incorporated.

Hence the complete system of equations from the model of Anderson et al. [18] describing the interactions of the tumour cells, ECM and MDEs is

$$\begin{aligned} \partial_t n &= \overbrace{\varepsilon \Delta n}^{\text{random motility}} - \overbrace{\nabla \cdot (n \chi \nabla c_1)}^{\text{haptotaxis}}, \\ \partial_t c_1 &= - \overbrace{\eta c_2 c_1}^{\text{degradation}}, \\ \partial_t c_2 &= \overbrace{d_2 \Delta c_2}^{\text{diffusion}} + \overbrace{\alpha n}^{\text{production}} - \overbrace{\beta c_2}^{\text{decay}}. \end{aligned} \quad (12)$$

This model is considered on the unit interval $\Omega = (0, 1)$ as well as on the unit square $\Omega = (0, 1)^2$. Zero-flux boundary conditions

$$\zeta \cdot (-\varepsilon \nabla n + n \chi \nabla c_1) = 0, \quad (13)$$

for the cells and

$$\zeta \cdot (-d_2 \nabla c_2) = 0, \quad (14)$$

for the MDEs are imposed on the boundaries of Ω where ζ is an appropriate outward unit normal vector. Suitable initial conditions are described in Sections 4.3.1 and 4.3.2 for the 1D and the 2D case, respectively.

Anderson et al. [18] undertook a range of simulation experiments based around the following set of parameter values:

$$\varepsilon = 0.001, \quad d_2 = 0.001, \quad \eta = 10, \quad \alpha = 0.1, \quad \beta = 0.5.$$

In order to explore the effect of the strength of haptotaxis on the invasive process they used a range of values ([0.005, 0.5]) for the haptotactic coefficient χ . In the following simulations we use values $\chi = 0.5$ and $\chi = 0.005$. Note that in the 1D simulations we use a value $\beta = 0$.

Prior to invasion, the tumour is a compact mass of cells with little or no local migration. Once invasion is triggered, the migration of the cells is very focused and direct. Hence in this paper we also consider the above system without random motion of the tumour cells, i.e.

$$\begin{aligned} \partial_t n &= -\nabla \cdot (n \chi \nabla c_1), \\ \partial_t c_1 &= -\eta c_2 c_1, \\ \partial_t c_2 &= d_2 \Delta c_2 + \alpha n - \beta c_2. \end{aligned} \quad (15)$$

2.3. Mathematical modelling of *Dictyostelium* aggregation

Biochemical oscillations in the slime mould *D. discoideum* (Dd) have been widely studied. An excellent comprehensive account of this process can be found in Weijer [22] and references contained therein. Periodic synthesis of pulses of cyclic AMP (cAMP) in Dd control chemotaxis and differentiation during aggregation of the amoebae after starvation. Supporting in vitro observations in agar show that the signalling system is capable of two types of dynamic behaviour: autonomous oscillations of cAMP and relay of suprathreshold cAMP pulses — the synthesis of a pulse of cAMP in response to external cAMP stimulation of sufficient magnitude. The chemotactic movement of the amoebae was first modelled by Keller and Segel and led to the classic Keller–Segel model of chemotaxis-driven instability [23].

Previous analysis [22] has demonstrated that relay and oscillations represent two modes of dynamic behaviour which stem from the autocatalytic regulation of adenylate cyclase, with the enzyme being activated upon binding of extracellular cAMP to a receptor on the surface of the cell. Relay is linked to autonomous oscillations and is a consequence of the excitability of the adenylate cyclase reaction in Dd.

Dd cells respond chemotactically to cAMP gradients and there is an internal signal transduction pathway involving cell receptors and cAMP and various other components. There have been several mathematical models in recent years (e.g. [24–30]) studying the chemotactic response coupled with the receptor dynamics. Many of these models can be

reduced to a system of three equations governing the evolution of Dd cell density n , the number/fraction of active cAMP receptors on the cell surface c_1 and the (external) cAMP concentration c_2 . These models take the generic form

$$\begin{aligned} \partial_t n &= \varepsilon \Delta n - \nabla \cdot (n \chi(c_1) \nabla c_2), \\ \partial_t c_1 &= F(c_1, c_2), \\ \partial_t c_2 &= \Delta c_2 + G(c_1, c_2, n). \end{aligned}$$

For a specific example we present the model of Höfer [31] who considers the system

$$\begin{aligned} \partial_t n &= \varepsilon \Delta n - \nabla \cdot \left(\chi_0 n \frac{c_1^m}{A^m + c_1^m} \nabla c_2 \right), \\ \partial_t c_1 &= -k_1 c_2 c_1 + k_2 (1 - c_1), \\ \partial_t c_2 &= \Delta c_2 + \alpha(n) \rho (b c_1 + c_1^2) \frac{a + c_2^2}{1 + c_2^2} - (\delta_1 \alpha(n) + \delta_2) c_2, \end{aligned} \tag{16}$$

on $\Omega = (0, 20)^2$ with

$$\alpha(n) = \begin{cases} \frac{n}{1.2 - n} & \text{if } n < 1 \\ 5 & \text{if } n \geq 1. \end{cases}$$

The parameter values estimated from experimental data were

$$\begin{aligned} \varepsilon = 0.012, \quad \chi_0 = 0.4, \quad A = 0.7, \quad m = 10, \quad \rho = 100, \quad a = 0.014, \\ b = 0.2, \quad \delta_1 = 23.5, \quad \delta_2 = 0.9, \quad k_1 = k_2 = 2.5. \end{aligned}$$

Once again, in the absence of cAMP waves, the Dd are relatively inert and there is little random motility. Once stimulated, the major response to cAMP is a chemotactic one, i.e. $\varepsilon \ll \chi_0$, and indeed Höfer et al. [24] comment that their cell equation is essentially “an advection equation with a small diffusive smoothing term”. Therefore, we also study the system in the absence of amoebae random motility, i.e. system (16) with parameter $\varepsilon = 0$:

$$\begin{aligned} \partial_t n &= -\nabla \cdot \left(\chi_0 n \frac{c_1^m}{A^m + c_1^m} \nabla c_2 \right), \\ \partial_t c_1 &= -k_1 c_2 c_1 + k_2 (1 - c_1), \\ \partial_t c_2 &= \Delta c_2 + \alpha(n) \rho (b c_1 + c_1^2) \frac{a + c_2^2}{1 + c_2^2} - (\delta_1 \alpha(n) + \delta_2) c_2. \end{aligned} \tag{17}$$

3. Numerical technique

In this section we describe in some detail the numerical techniques which we apply to obtain approximate solutions of system (3) for $\Omega = (0, 1)^2$. A restriction to 1D or a generalisation to higher space dimensions is straightforward. We follow the method of lines (MOL) approach. This means that as a first step we replace the spatial derivatives in the PDE system by, in our approach, a finite volume approximation on a spatial grid. The result is a large, in general stiff, system of ordinary differential equations (ODEs). This so-called MOL-ODE is then integrated in time using an appropriate method in a second step. Hence, finally we obtain approximations to the solution of (3) on a discrete spatial and temporal grid. A comprehensive treatment of theoretical and practical issues of numerical methods for advection–diffusion–reaction equations (accuracy and stability of schemes, computational costs, etc.) may be found in the excellent monograph by Hundsdorfer and Verwer [32]. This book also contains biomedical applications. A more general discussion of mathematical modelling and computational issues regarding biological systems may be found in the book by Bellomo and Preziosi [33].

We have the unit square $\Omega := (0, 1)^2$ as our computational domain and cover it by an equi-spaced linear grid with M computational cells in each spatial direction. The width of such a cell is denoted by $h := 1/M$ and we assume cell-centred grid points. Hence we have grid cells $\Omega_i := ((i_1 - 1)h, i_1 h) \times ((i_2 - 1)h, i_2 h)$ and corresponding grid

points $\mathbf{x}_i := ((i_1 - 1/2)h, (i_2 - 1/2)h)$ for multi-indices $\mathbf{i} = (i_1, i_2) \in \mathcal{I} := \{1, 2, \dots, M\} \times \{1, 2, \dots, M\}$. The set $\{\Omega_i\}_{i \in \mathcal{I}}$ forms a partition of Ω . For convenience of notation we assume that the grid is extended beyond the boundary of Ω in an analogous fashion.

3.1. Discretization in space

We now describe the approximations of the spatial derivatives in Eq. (3) by a finite volume technique. An exact evolution equation for the cell averages of n and \mathbf{c} underlies Eq. (3) (see [7]) and this evolution equation is the starting point for the finite volume discretization. The cell average of n in Ω_i (and analogously for the components of \mathbf{c}) is defined by

$$\bar{n}_i(t) := \frac{1}{|\Omega_i|} \int_{\Omega_i} n(t, \mathbf{x}) \, d\mathbf{x}.$$

For simplicity of presentation we describe the spatial discretization only for the TDR equation for n ; then the corresponding discretization of the \mathbf{c} -part of (3) follows easily. The evolution of the cell average $\bar{n}_i(t)$ is exactly governed by ($\zeta = \zeta(\mathbf{x})$ is the unit outward normal vector in $\mathbf{x} \in \partial\Omega_i$)

$$\frac{d\bar{n}_i}{dt} = \underbrace{\frac{1}{|\Omega_i|} \oint_{\partial\Omega_i} \varepsilon \nabla n \cdot \zeta \, d\partial\Omega_i}_{=: H_D(n(t, \cdot); \mathbf{i})} - \underbrace{\frac{1}{|\Omega_i|} \oint_{\partial\Omega_i} n \left(\sum_{j=1}^l p_j(\mathbf{c}) \nabla c_j \right) \cdot \zeta \, d\partial\Omega_i}_{=: H_T(n(t, \cdot); \mathbf{i})} + \underbrace{\frac{1}{|\Omega_i|} \int_{\Omega_i} f_0(n, \mathbf{c}) \, d\mathbf{x}}_{=: H_R(n(t, \cdot); \mathbf{i})}. \quad (18)$$

We denote by $H(n(t, \cdot); \mathbf{i})$ the right-hand side of the exact cell average Eq. (18). It may depend on n at time t over the whole domain Ω (we denote this by $n(t, \cdot)$), and also on $\mathbf{c}(t, \cdot)$ (which is suppressed in the notation). Further, H_D , H_T , and H_R are the parts of H corresponding to diffusion, taxis, and reaction, respectively. In short we write for the above equation

$$\frac{d}{dt} \bar{n}_i(t) = H(n(t, \cdot); \mathbf{i}) \equiv H_D(n(t, \cdot); \mathbf{i}) + H_T(n(t, \cdot); \mathbf{i}) + H_R(n(t, \cdot); \mathbf{i}). \quad (19)$$

Henceforth we denote by $N_i(t)$ an approximation to the cell average $\bar{n}_i(t)$ and collect the approximations for all cells of the partition in the vector $\mathbf{N}(t)$. Similarly, for each concentration c_j , we collect the approximate averages $C_{j,i}$ in a vector $\mathbf{C}_j(t)$ and also define $\mathbf{C}_{\cdot, \mathbf{i}} := [C_{1, \mathbf{i}}, C_{2, \mathbf{i}}, \dots, V_{l, \mathbf{i}}]$. (We can regard these values also as approximations of $n(t, \mathbf{x}_i)$ and $c_j(t, \mathbf{x}_i)$ in the cell centres \mathbf{x}_i .)

The idea of the finite volume approach is to approximate the right-hand side of Eq. (19) by using cell averages of n (and c_j) in neighbouring cells of Ω_i . Let $\mathcal{H}(\mathbf{N}(t); \mathbf{i})$ be an approximation to $H(n(t, \cdot); \mathbf{i})$ which depends on a finite number of elements of $\mathbf{N}(t)$ (and possibly on a finite number of components of $\mathbf{C}_j(t)$, $j = 1, 2, \dots, l$). Then we obtain an ODE system for the evolution of the approximate cell averages:

$$\frac{d}{dt} N_i(t) = \mathcal{H}(\mathbf{N}(t); \mathbf{i}), \quad \mathbf{i} \in \mathcal{I}, \quad (20)$$

the so-called MOL-ODE. The initial values for this ODE are provided as approximations \mathbf{N}_0 to the cell averages of a given initial condition for n in Ω . In the following we describe appropriate approximations \mathcal{H}_D , \mathcal{H}_T , and \mathcal{H}_R to H_D , H_T , and H_R , respectively. The right-hand side of the MOL-ODE (20) is then defined as $\mathcal{H}(\mathbf{N}(t); \mathbf{i}) := \mathcal{H}_T(\mathbf{N}(t); \mathbf{i}) + \mathcal{H}_D(\mathbf{N}(t); \mathbf{i}) + \mathcal{H}_R(\mathbf{N}(t); \mathbf{i})$.

For $\mathcal{H}_R(\mathbf{N}(t); \mathbf{i})$ we choose

$$\mathcal{H}_R(\mathbf{N}(t); \mathbf{i}) := f_0(N_i, \mathbf{C}_{\cdot, \mathbf{i}}).$$

This results in a first-order accurate approximation in the finite volume sense. In a pointwise interpretation it is just the exact evaluation of the reaction function f_0 in the cell centre.

It remains to define $\mathcal{H}_D(\mathbf{N}(t); \mathbf{i})$ and $\mathcal{H}_T(\mathbf{N}(t); \mathbf{i})$ by approximating the surface integrals in Eq. (19). We can dimensionally split these integrals because of the structure of the grid cells Ω_i and we define (\mathbf{e}_k is the k th unit vector)

$$\mathcal{H}_D(\mathbf{N}(t); \mathbf{i}) := \frac{1}{h} \sum_{k=1}^2 (\mathcal{D}_k(\mathbf{N}(t); \mathbf{i}) - \mathcal{D}_k(\mathbf{N}(t); \mathbf{i} - \mathbf{e}_k)), \tag{21}$$

$$\mathcal{H}_T(\mathbf{N}(t); \mathbf{i}) := -\frac{1}{h} \sum_{k=1}^2 (\mathcal{T}_k(\mathbf{N}(t); \mathbf{i}) - \mathcal{T}_k(\mathbf{N}(t); \mathbf{i} - \mathbf{e}_k)). \tag{22}$$

Here, $\mathcal{D}_k(\mathbf{N}(t); \mathbf{i})$ approximates the average of the negative diffusive flux from $\Omega_{\mathbf{i}}$ to $\Omega_{\mathbf{i}+\mathbf{e}_k}$ through their common cell face $\Gamma := \bar{\Omega}_{\mathbf{i}} \cap \bar{\Omega}_{\mathbf{i}+\mathbf{e}_k}$, i.e.

$$\mathcal{D}_k(\mathbf{N}(t); \mathbf{i}) \approx \frac{1}{h} \int_{\Gamma} \varepsilon \partial_{x_k} n(t, \mathbf{x}) d\Gamma.$$

Similarly, $\mathcal{T}_k(\mathbf{N}(t); \mathbf{i})$ approximates the average of the taxis flux from $\Omega_{\mathbf{i}}$ to $\Omega_{\mathbf{i}+\mathbf{e}_k}$, i.e.

$$\mathcal{T}_k(\mathbf{N}(t); \mathbf{i}) \approx \frac{1}{h} \int_{\Gamma} n(t, \mathbf{x}) \left(\sum_{j=1}^l p_j(\mathbf{c}(t, \mathbf{x})) \partial_{x_k} c_j(t, \mathbf{x}) \right) d\Gamma.$$

We note that for some $\mathbf{i} \in \mathcal{I}$ the definitions of \mathcal{H}_D and \mathcal{H}_T refer to grid cells, which are adjacent to but not part of Ω . In these cases we have to construct flux approximations \mathcal{D}_k and \mathcal{T}_k by using the prescribed boundary data of the models. For the specific treatment we refer to [7]. Here we will concentrate on grid cells away from the boundary. The definitions of \mathcal{H}_D and \mathcal{H}_T are in conservation form. This implies that, for $f_0 \equiv 0$, the temporal change of discrete total mass in Ω , $\frac{d}{dt} h^2 \sum_{\mathbf{i} \in \mathcal{I}} N_{\mathbf{i}}(t)$, depends only on fluxes through $\partial\Omega$. This mimics the conservation of mass property of the underlying conservation law for n . Discretizations in conservation form are also important for the treatment of nonlinear systems of hyperbolic conservation laws; see e.g. [6]. It remains to compute the approximations \mathcal{D}_k and \mathcal{T}_k . Henceforth we neglect the t dependence of $\mathbf{N}(t)$ and $\mathbf{C}_j(t)$ in the notation.

We define the approximate negative diffusive flux by

$$\mathcal{D}_j(\mathbf{N}; \mathbf{i}) := \frac{\varepsilon}{h} (N_{\mathbf{i}+\mathbf{e}_j} - N_{\mathbf{i}}). \tag{23}$$

Substituting this into (21) leads, in a pointwise interpretation, to the standard second-order central difference approximation of the diffusion operator. Further, we also obtain a second-order approximation of the evolving cell averages in the finite volume sense.

The definition of the approximate taxis fluxes is a bit more difficult. We follow the state interpolation approach to define the approximations $\mathcal{T}_k(\mathbf{N}; \mathbf{i})$. This is based on work by Hundsdorfer et al. [34]. A possible flux interpolation approach (for a specific TDR system) is described in [35]. First we compute an average velocity $v_{\mathbf{i},k}$ on the cell face $\Gamma := \bar{\Omega}_{\mathbf{i}} \cap \bar{\Omega}_{\mathbf{i}+\mathbf{e}_k}$ using

$$v_{\mathbf{i},k} := \sum_{j=1}^l p_j \left(\frac{\mathbf{C}_{\cdot,\mathbf{i}} + \mathbf{C}_{\cdot,\mathbf{i}+\mathbf{e}_k}}{2} \right) \frac{C_{j,\mathbf{i}+\mathbf{e}_k} - C_{j,\mathbf{i}}}{h}. \tag{24}$$

Note that the taxis functions p_j are evaluated on Γ . The definition of the approximate taxis flux through Γ depends on the sign of this velocity, i.e. it is dependent on the flow direction. This technique is called *upwinding* and it is standard in the discretization of advection terms. The taxis term in our models can be regarded as nonlinear advection. We approximate the taxis flux by

$$\mathcal{T}_k(\mathbf{N}; \mathbf{i}) := \max\{0, v_{\mathbf{i},k}\} \mathcal{S}_k^+(\mathbf{N}; \mathbf{i}) + \min\{0, v_{\mathbf{i},k}\} \mathcal{S}_k^-(\mathbf{N}; \mathbf{i}). \tag{25}$$

The state interpolants $\mathcal{S}_k^+(\mathbf{N}; \mathbf{i})$ and $\mathcal{S}_k^-(\mathbf{N}; \mathbf{i})$ approximate the average value (state) of n on Γ . If we choose the state interpolants to be linear combinations of components of \mathbf{N} (e.g. leading to a second-order central discretization) then we can achieve an approximation order greater than one but the resulting discretizations would introduce unphysical oscillations near steep gradients in the solution; see [34,36]. These oscillations could lead to negative solution values (although a density is modelled) and negative solution values might turn stable reactions (f_0, \mathbf{g}_0) into unstable ones and therefore they are highly undesirable. (We return to the topic of *positivity* at the end of this section.) We want

to combine a higher approximation order with *positivity* and therefore use so-called limiter functions $\Phi(r)$ in the definition of the state interpolants:

$$S_k^+(\mathbf{N}; \mathbf{i}) := \begin{cases} N_{\mathbf{i}} + \frac{1}{2} \Phi(r_{\mathbf{i},k})(N_{\mathbf{i}} - N_{\mathbf{i}-\mathbf{e}_k}) & \text{for } N_{\mathbf{i}} - N_{\mathbf{i}-\mathbf{e}_k} \neq 0 \\ N_{\mathbf{i}} & \text{otherwise,} \end{cases} \quad (26a)$$

$$S_k^-(\mathbf{N}; \mathbf{i}) := \begin{cases} N_{\mathbf{i}+\mathbf{e}_k} + \frac{1}{2} \Phi(r_{\mathbf{i}+\mathbf{e}_k,k}^{-1})(N_{\mathbf{i}+\mathbf{e}_k} - N_{\mathbf{i}+2\mathbf{e}_k}) & \text{for } N_{\mathbf{i}+\mathbf{e}_k} - N_{\mathbf{i}+2\mathbf{e}_k} \neq 0 \\ N_{\mathbf{i}+\mathbf{e}_k} & \text{otherwise.} \end{cases} \quad (26b)$$

We require that the limiter function $\Phi(r)$ is Lipschitz continuous, so that we obtain a Lipschitz continuous discretization altogether (provided the data of problem (3) are Lipschitz). The limiter Φ depends on a *smoothness monitor function* r which we define for the grid function \mathbf{N} by

$$r_{\mathbf{i},k} := \frac{N_{\mathbf{i}+\mathbf{e}_k} - N_{\mathbf{i}}}{N_{\mathbf{i}} - N_{\mathbf{i}-\mathbf{e}_k}}. \quad (27)$$

We see that $r_{\mathbf{i},k} \approx 1$ in smooth, monotone regions of \mathbf{N} along the k th coordinate direction and $r_{\mathbf{i},k} < 0$ if $N_{\mathbf{i}}$ is a local extremum of \mathbf{N} in the k th coordinate direction.

Finally, we give two limiter functions which we will use in our numerical tests. There are more functions available in the literature; see e.g. [37,34,38]. We use either the van Leer limiter Φ_{VL} or the Koren limiter Φ_K , defined by

$$\Phi_{VL}(r) := \frac{r + |r|}{1 + |r|} \quad \text{and} \quad \Phi_K(r) := \max \left\{ 0, \min \left\{ 2r, \delta, \frac{1}{3} + \frac{2}{3}r \right\} \right\}, \quad \delta = 2.$$

Choosing $\Phi \equiv 0$ leads to the standard first-order upwind discretization. We do not use this discretization for the simulation of TDR systems because, due to its diffusive character, it requires an excessive amount of grid cells in order to achieve an acceptable spatial accuracy. We see that $\Phi_{VL}(r_{\mathbf{i},k})$ and $\Phi_K(r_{\mathbf{i},k})$ switch back to this first order if $N_{\mathbf{i}}$ is a local extremum in coordinate direction k . The choice $\delta = 2$ is discussed in [34] and we refer the reader to this paper for details.

If $\Phi(1) = 1$, then the order of the taxis approximation $\mathcal{H}_T(\mathbf{N}; \mathbf{i})$, in the pointwise interpretation, is two in uniform flow regions away from local extrema of the solution n . The given limiter functions Φ_{VL} and Φ_K satisfy this condition.

Finally, we return to the question of positivity. The ODE system (20) is called *positive* if it has a solution for any choice of initial data $\mathbf{N}(t_0)$, and this solution remains nonnegative for all times $t > t_0$ provided that $\mathbf{N}(t_0) \geq 0$. If the reaction functions f_0, \mathbf{g}_0 are Lipschitz continuous then, in our case, the solution of (20) exists always because the limiter Φ is also Lipschitz continuous. Following Horvath [39] (see also [34]), the system (20) is then positive if and only if for arbitrary $\mathbf{N} \geq 0$ (and all possible values of \mathbf{C}_j) it holds that

$$N_{\mathbf{i}} = 0 \Rightarrow \mathcal{H}(\mathbf{N}, \mathbf{i}) \geq 0.$$

It can be shown (see [7]) that this condition is satisfied for the described discretization in space (and suitable boundary treatment) if $f_0(0, \mathbf{C}_{\cdot,\mathbf{i}}) \geq 0$ for all possible values of $\mathbf{C}_{\cdot,\mathbf{i}}$.

To summarise, we have now discretized system (3) and obtained a positive MOL-ODE of the form (20). In the next section we describe methods which integrate this system efficiently in time.

3.2. Time stepping

The result of the spatial discretization of system (3) is an initial value problem for a huge system of stiff, nonlinear ODEs, the MOL-ODE, which remains to be numerically integrated in time. We denote the MOL-ODE by

$$y'(t) = F(t, y(t)), \quad y(0) = y_0, \quad t \in [0, T]. \quad (28)$$

Hence the solution vector y is the grid function containing all semi-discrete approximations to (the cell averages of) the population density n and the chemicals c_j . We are especially interested in the numerical integration of these large ODE systems by means of splitting techniques. The usefulness of splitting techniques becomes evident when we write the vector function F as

$$F(t, y) = F_0(t, y) + F_1(t, y), \quad (29)$$

0	0	0	0	0	0
1	0	1	0	1/2	0
1/2	1/2	1/4	1/4	1/2	1/2
1/2	1/2	1/6	1/6	2/3	2/3

Fig. 1. Butcher arrays of the methods ME, RKF2(3), and RK32 (left to right).

where we have collected all terms from the taxis discretization in F_0 and all diffusion and reaction terms in F_1 . We separate these terms because the system $y'(t) = F_1(t, y(t))$ generally requires an implicit treatment because of stiffness, whereas the semi-discrete taxis system $y'(t) = F_0(t, y(t))$ is better solved explicitly because this is often more efficient. Using low order explicit Runge–Kutta (ERK) methods and linearly implicit Runge–Kutta–Rosenbrock methods, we employ two splitting techniques, operator splitting (OPS) and approximate matrix factorization (AMF). For a more detailed discussion of these schemes we refer the reader to [40]. The splitting techniques OPS and AMF make use of the separation and treat F_0 and F_1 differently. We can further split F_1 by separating terms of x_1 - and x_2 -diffusion discretization and reaction terms,

$$F_1(t, y) = F_{D_{x_1}}(t, y) + F_{D_{x_2}}(t, y) + F_R(t, y). \tag{30}$$

This secondary splitting is used to reduce linear algebra costs.

The numerical methods generate approximations y_n to $y(t_n)$ from y_{n-1} , $n = 1, 2, \dots$, in a step-by-step fashion. Let $\tau_n := t_{n+1} - t_n$ ($t_0 := 0$) denote the size of a time step (we neglect the subscript on τ for ease of notation).

3.2.1. An ERK method for the taxis part of the MOL-ODE

We stated that $y'(t) = F_0(t, y(t))$ is efficiently solved with explicit methods. Further, it is important that we obtain a nonnegative numerical approximation y_n using suitably large time steps τ for efficiency reasons. This is particularly difficult for the taxis ODE considered here because of the steep gradients present in the cell density solution (we have $F_{0,i} \neq 0$ only for components i of y which correspond to cell density approximations). Positivity properties of low order ERK methods applied to linear and nonlinear classes of positive ODEs are studied in [41]. A three-stage, second-order ERK method (RK32) with favourable positivity and stability properties and good numerical performance is singled out. Another suitable method with respect to positivity, accuracy, and efficiency is the two-stage, second-order modified Euler method (ME). The Butcher arrays defining both methods are given in Fig. 1.

Numerical experiments in [41] show that ME and RK32 perform comparably when solving a semi-discretized (upwinding with a van Leer limiter) linear advection equation in one spatial dimension,

$$\partial_t n(t, x_1) + a \partial_{x_1} n(t, x_1) = 0, \quad a > 0. \tag{31}$$

Further experiments in [41] and also in [40] show that splitting methods for the full system (28) which are based on RK32 perform more satisfactorily than the same methods based on ME.

In [34] the maximum value of $\nu := \frac{a\tau}{h}$ for which it is guaranteed that ERK methods yield nonnegative approximations of the solution of the MOL-ODE (van Leer or Koren limiter) for Eq. (31) is investigated. Combining this with the results in [41] it follows that $\nu = 0.5$ for ME (and also for the three-stage, third-order ERK method RKF2(3) considered in both papers), and $\nu = 1$ for RK32, i.e. the allowable time step size for positivity is doubled.

Next we will study the linear stability properties of ME and RK32 (and RKF2(3)) when applied to semi-discretizations of Eq. (31). If we apply the described taxis discretization with limiters Φ_{VL} or Φ_K , then we obtain a nonlinear MOL-ODE. For smooth solutions, we can linearise the limiter functions around $r = 1$. This yields the linear limiter functions

$$\Phi_{VL}^L(r) = K_0(r), \quad \Phi_K^L(r) = K_{1/3}(r), \quad \text{where } K_\kappa(r) = \frac{1 - \kappa}{2} + \frac{1 + \kappa}{2}r,$$

and we obtain subsequently a linear MOL-ODE. The discretizations obtained belong to the κ -family [34] and Φ_K^L leads to a third-order scheme, whereas Φ_{VL}^L leads to a second-order one. If we assume periodic boundary conditions for

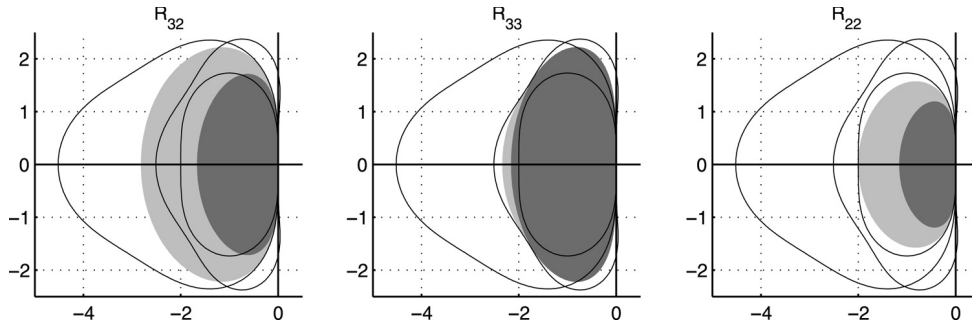


Fig. 2. The lines in each of the plots are the boundaries of the stability domains of methods with stability polynomials $R_{3,2}$, $R_{3,3}$, and $R_{2,2}$ (from largest to smallest; the stability domain is the respective interior area). The dark grey shaded area in each plot is the stability region of methods with stability polynomial as given in the plot title if the eigenvalues are confined to $\lambda_{1/3}(\xi)$, i.e. the limiter function Φ_K^L (the light grey shaded area corresponds to eigenvalues $\lambda_0(\xi)$, i.e. the limiter function Φ_{VL}^L).

Eq. (31) then we can apply Fourier analysis (see e.g. [42]). The complex eigenvalues $\lambda_\kappa(\xi)$ for the spatial discretization with limiter function $K_\kappa(r)$ (derived as explained in e.g. [43]) are, for $\xi \in [-\pi, \pi]$,

$$\lambda_\kappa(\xi) = -\frac{|a|}{h} \frac{1-\kappa}{2} \left((\cos \xi - 1)^2 + i \operatorname{sign}(a) \sin \xi \left(\frac{3-\kappa}{1-\kappa} - \cos \xi \right) \right).$$

We see that Φ_{VL}^L introduces slightly more damping into the numerical scheme than Φ_K^L because the corresponding eigenvalues $\lambda_0(\xi)$ have a more negative real part. (A Fourier analysis of (31) yields purely imaginary eigenvalues, i.e. there is no damping at all.) The $\lambda_\kappa(\xi)$ eigenvalues multiplied by the time step τ are now substituted in the stability polynomials

$$R_{2,2}(z) = 1 + z + \frac{z^2}{2}, \quad R_{3,2}(z) = R_{2,2}(z) + \frac{z^3}{12}, \quad \text{and} \quad R_{3,3}(z) = R_{2,2}(z) + \frac{z^3}{6},$$

of ME, RK32 and three-stage, third-order ERK methods, respectively. For stability it is required that the absolute value of the stability polynomial is less than one for given values of h and τ and all $\xi \in [-\pi, \pi]$. We compute numerically the maximum value of ν such that this condition is satisfied. Then we obtain for the eigenvalues $\lambda_{1/3}(\xi)$ the approximate values $\nu_{2,2} = 0.87$, $\nu_{3,2} = 1.26$, $\nu_{3,3} = 1.62$ and for $\lambda_0(\xi)$ the approximate values $\nu_{2,2} = 1$, $\nu_{3,2} = 1.41$, $\nu_{3,3} = 1.17$. The corresponding stability regions are depicted in Fig. 2. We see that the RK32 method allows for the largest time steps (with respect to stability) if we use the linearised van Leer limiter. This, together with the good positivity properties, makes RK32 our favourite candidate for the solution of the taxis ODE. This choice is backed up by numerical results presented in [41,40].

3.2.2. Rosenbrock AMF methods

Verwer et al. [44] successfully applied the two-stage, second-order Rosenbrock-W method ROS2 to advection–diffusion–reaction problems from atmospheric air pollution modelling. The same method is studied in [40] for application to semi-discretized TDR models. Because our current models give rise to autonomous systems, we consider for ROS2 the autonomous form

$$\begin{aligned} y_{n+1} &= y_n + \tau \left(\frac{3}{2}k_1 + \frac{1}{2}k_2 \right), \\ y_{n+1}^{(1)} &= y_n + \tau k_1, \\ (I - \tau\gamma A)k_1 &= F(y_n), \\ (I - \tau\gamma A)k_2 &= F(y_{n+1}^{(1)}) - 2k_1. \end{aligned} \tag{32}$$

Here A is an arbitrary approximation to the Jacobian matrix $F'(y_n)$. If we take for A the zero matrix, then ROS2 reduces to the ME method. We have second-order consistency for any matrix A (the so-called *W-method property*) and any value of the parameter $\gamma > 0$. A -stability of the method is given for $\gamma \geq \frac{1}{4}$ and L -stability is obtained for

$\gamma = 1 \pm \sqrt{2}/2$. In [5] it is observed that L -stable integration schemes are necessary for the stable simulation of a specific TDR model. With this result in mind, and from our own experience (and for positivity reasons) we select the smaller value $\gamma = 1 - \sqrt{2}/2$. The auxiliary value

$$y_{n+1}^{(1)} = y_n + \tau k_1$$

provides a first-order embedded solution which will be used for variable time step size control.

For stability and accuracy reasons we would like to apply the method with exact Jacobian $A = F'(y_n)$. This Jacobian is broadly banded in our case and therefore the two linear system solves per step of ROS2 become prohibitively expensive. This is especially true for the fine spatial resolution which is required in our model in order to resolve the steep fronts in the cell density approximation. In order to find a suitable approximation of $F'(y_n)$ we first neglect the taxis part F_0 in the Jacobian. This choice underlies the assumption that the ME method, when applied to $y' = F_0(y)$, has satisfactory positivity and stability properties. The remaining F_1 -part of the right-hand side of the MOL-ODE is used to define the matrix A . Here, the secondary splitting (30) comes into play in order to reduce the linear algebra costs. We define A such that

$$I - \tau\gamma A = (I - \tau\gamma F'_R(y_n))(I - \tau\gamma F'_{D_{x_2}}(y_n))(I - \tau\gamma F'_{D_{x_1}}(y_n)). \tag{33}$$

The matrices in the factorization have small band widths (independent of the spatial grid size) for a suitable arrangement of the components in y , and the linear systems in the ROS2 method can be solved efficiently. The factorization is known as ‘Approximate Matrix Factorization’ (AMF) which has been in use for a long time already for solving multi-space dimensional time dependent PDE problems; see [45] for a survey. AMF does not affect the order of consistency because ROS2 is of second order for any choice of A . It does of course affect the stability of the original ROS2 used with $A = F'(y_n)$. In [44] it is argued that with (33) the stability of the resulting AMF-ME method is mainly governed by the stability of the method ME applied to the advection part only. A similar conclusion can be drawn for the taxis–diffusion–reaction problems. If the split matrices do not commute then the order of the factors in the AMF can be important for the performance of the method and the best choice is problem specific. We refer to the described method as AMF-ME.

In the previous subsection we have recommended the ERK method RK32 because it allows for larger time steps than ME in applications to $y' = F_0(y)$. With this observation in mind, a three-stage, second-order RK-Rosenbrock-W method with underlying ERK method RK32 is constructed in [40]. The method is L -stable and third-order accurate for linear problems. We can also apply AMF to this method and refer to the resulting method as AMF-RK32.

3.2.3. Operator splitting methods

Whereas the AMF methods perform a splitting at the linear algebra level, it is also possible to directly split at the problem level, that is, to apply operator splitting. Like approximate factorization, operator splitting is a popular approach for solving multi-space dimensional time dependent PDE problems. Operator splitting has been considered in [35] for a tumour angiogenesis model. The method proceeds as follows. Given an approximation y_n at time t_n and a step size τ , we compute

$$y_{n+1} = \Psi_0\left(\frac{\tau}{2}, t_n + \frac{\tau}{2}\right) \Psi_1(\tau, t_n) \Psi_0\left(\frac{\tau}{2}, t_n\right) y_n, \tag{34}$$

where Ψ_0 and Ψ_1 are approximate evolution operators of F_0 and F_1 , respectively. Specifically, $\Psi_i(\tau, \tilde{t})u$ approximates the solution of the initial value problem (here in non-autonomous form)

$$y'(t) = F_i(t, y(t)), \quad t \geq \tilde{t}, \quad y(\tilde{t}) = u,$$

at $t = \tilde{t} + \tau$. This form is known as Strang-splitting [46]. If the operators Ψ_i are at least second-order accurate approximations of the exact evolution operators, then the order of consistency of the approximation (34) equals two. The stability and positivity of (34) is determined by the associated properties of Ψ_0 and Ψ_1 .

It is effective to select an explicit method for Ψ_0 and an implicit method for Ψ_1 . We have already all necessary ingredients available and will use the ROS2 scheme with AMF for the implicit method (see Section 3.2.2 and replace F by F_1 in the method (32)). The explicit method will be either ME or RK32. We refer to the resulting operator splitting schemes as OPS-ME and OPS-RK32, respectively. Operator splitting is applied in the order given in (34)

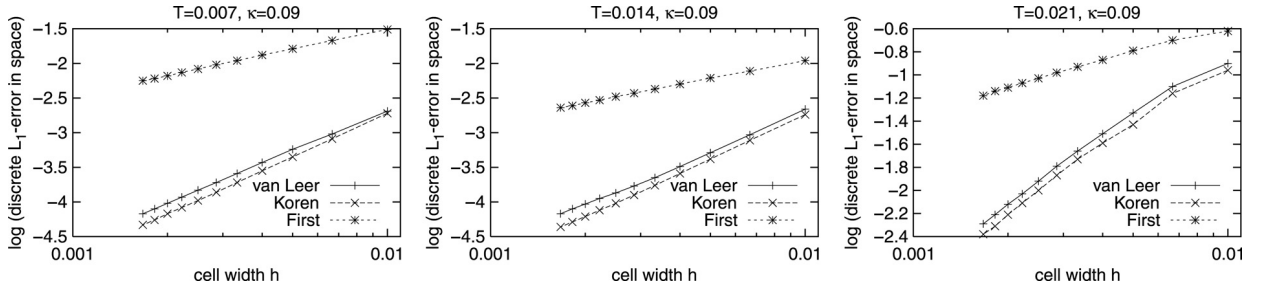


Fig. 3. Plots of the logarithm of the measured $\|\cdot\|_1$ -error against the cell width h for different limiter functions and final times T (left to right) for the test model and smooth initial data ($\varepsilon = 0.09$).

because then we use only half the step size of the splitting step for the explicit method. This doubles the stability and positivity domain of the explicit method and hence is expected to lead overall to fewer time steps.

4. Numerical experiments and simulations

We have implemented the spatial discretization of the models and also the time integration schemes in FORTRAN77. We use a standard time step size control (see e.g. [47]) in the time integration schemes in order to have some control over the integration errors in time. The spatial discretization of the models is done on grids with constant grid width $h = 1/100$ in each spatial direction (if not indicated otherwise in the following sections).

4.1. Evaluation of the spatial discretization of the taxis part

In this section we present numerical simulations and experiments which confirm that the spatial discretization of the taxis part of our models (described in the previous section) is appropriate. We investigate whether the expected order of convergence (two) is attained numerically, and we also discuss the different results obtained with different limiter functions Φ . The model from Section 2.1 is a suitable test model for this purpose because we have an analytic solution of this problem. Further, this solution is radially symmetric and we want the numerical approximation to share (approximately) the same qualitative property. Other qualitative tests are the conservation of mass and the nonnegativity property of the solution of the test model.

We discretize the taxis term with the state interpolation approach and use three limiter functions: van Leer Φ_{VL} , Koren Φ_K , and first-order $\Phi_1 := 0$, and obtain the MOL-ODE. (Note that the computations are executed on the unit square domain and no advantage is taken from assuming that the solution is radially symmetric.)

We are concerned with comparing the exact solution $n(t, \mathbf{x})$ of the test model with the exact solution $\mathbf{N}(t)$ of the MOL-ODE in some norm. We do not know the exact solution of the MOL-ODE and therefore it has to be obtained numerically. For this purpose we employ the standard ODE solver DOPRI5 [47] with sufficiently high accuracy that the errors of the time integration become negligible compared to the spatial errors introduced by the discretization in space. We regard the (DOPRI5) result as the exact solution of the MOL-ODE and denote it with $\mathbf{N}(t)$.

On the other hand, we know the exact (PDE) solution of the test model and define a reference solution $\mathbf{N}_{\text{ref}}(t)$ by $N_{\text{ref},i} := n(t, \mathbf{x}_i)$ for all $i \in \mathcal{I}$. We measure the difference $\mathbf{E} := \mathbf{N}(t) - \mathbf{N}_{\text{ref}}(t)$ between the two vectors in the discrete L^1 -norm $\|\cdot\|_1$,

$$\|\mathbf{E}\|_1 := \sum_{i \in \mathcal{I}} |\Omega_i| |E_i|. \quad (35)$$

We start with assessing the numerical order of convergence of our discretization in space and therefore choose the smooth initial function (5) with $\varepsilon = 0.09$. Then the solution of the model is also smooth. We note, however, that the gradients in the solution become steeper with increasing time. For this reason, we consider three final times, $T_1 = 0.007$, $T_2 = 0.014$, and $T_3 = 0.021$ (see also the paper by Tyson et al. [5], where the same final times for this model are considered). We compute the solution on the sequence of partitions of Ω with grid widths $h = h_k := \frac{1}{50k}$, $k = 2, 3, \dots, 12$. In Fig. 3 we plot the logarithm of the measured $\|\cdot\|_1$ -error obtained with the van Leer Φ_{VL} , Koren Φ_K , and first-order Φ_1 limiter functions versus the cell width h for three final times T (left to right).

Table 1
Orders of convergence p and error constants C corresponding to the plots of Fig. 3

	$T = 0.007$		$T = 0.014$		$T = 0.021$	
	C	p	C	p	C	p
Φ_{VL}	14.07	1.91	144.52	1.93	781.16	1.85
Φ_K	26.55	2.07	276.04	2.09	799.18	1.89
Φ_1	2.63	0.96	6.43	0.88	7.90	0.74

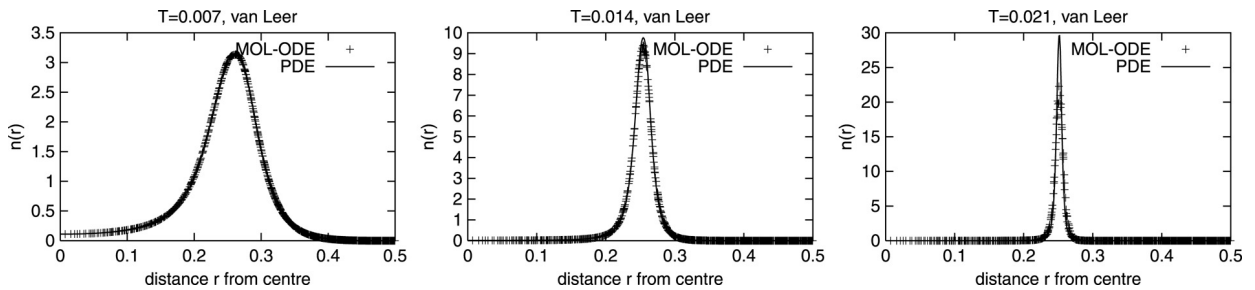


Fig. 4. Values of the analytical solution of the test model (4) and (5) with smooth initial data ($\varepsilon = 0.09$) and of the corresponding MOL-ODE (with van Leer limiter) at three different final times T (left to right) plotted against the distance r between the grid point and the centre of the unit square. The spatial resolution is $h = 1/100$. (The results with the Koren limiter (not given here) are almost indistinguishable from the results with the van Leer limiter.)

The corresponding (numerical) orders of convergence p and the error constants C are computed by a least squares procedure such that $err_k \approx Ch_k^p$, where the error err_k is attained on the grid with cell width h_k . They are listed in Table 1.

We see that the discretizations converge to the analytic solution but immediately recognise that the first-order scheme cannot compete with the limited higher order discretizations. The error attained with the first-order scheme on the finest grid is of the size of the error of the second-order discretizations on the coarsest grid. Hence, the application of the first-order discretization for the taxis term in our more complex biomathematical models would require extremely fine meshes to achieve sufficient spatial resolution but this is not feasible in view of the implied computational effort. Therefore we do not consider the first-order spatial discretization of the flux terms for these models. Comparing the errors of the higher order discretizations we see that the discretizations using the Koren limiter are slightly more accurate than that using the van Leer limiter. The numbers in Table 1 show that these two discretizations almost attain the theoretical order two in the $\|\cdot\|_1$ -norm. We note that the error constants C grow very large for increasing final time T .

The discretizations with all three limiter functions yield nonnegative solutions at final time (at least for the high temporal accuracy requested in the experiments here). Further, the mass of the solution is conserved up to machine accuracy in all experiments.

Finally, we look at the symmetry of the solution of the MOL-ODE. We therefore plot, for a fixed value of t , all solution points $(\mathbf{x}_i, N_i(t))$, $\mathbf{i} \in \mathcal{I}$, as points $(r(\mathbf{x}_i), N_i(t))$ in a diagram. We plot the analytic PDE solution (6) of the test model (4) and (5) at time t in the same manner in this diagram, and since the PDE solution is radially symmetric, this corresponds to a single solution line in the diagram. In Fig. 4 we present some of these diagrams (for details see the caption there). We see that the solution points of the MOL-ODE are close to the solution line of the PDE. Further, for a fixed value of r , there is no scattering of solution points of the MOL-ODE around the solution value of the PDE for r . This indicates also that the solution of the MOL-ODE is radially symmetric.

We now turn our attention to a discontinuous initial condition ($\varepsilon = 0$) in the test model. We give plots of the spatial error in the $\|\cdot\|_1$ -norm against the cell width (see Fig. 5), and the corresponding orders and error constants in Table 2.

The same comments as were made for smooth initial data apply as regards the first-order scheme. For the higher order methods we observe that the differences are almost negligible. The order of convergence of the discretizations is clearly less than the theoretical order but this is expected and due to missing spatial smoothness of the solution; see

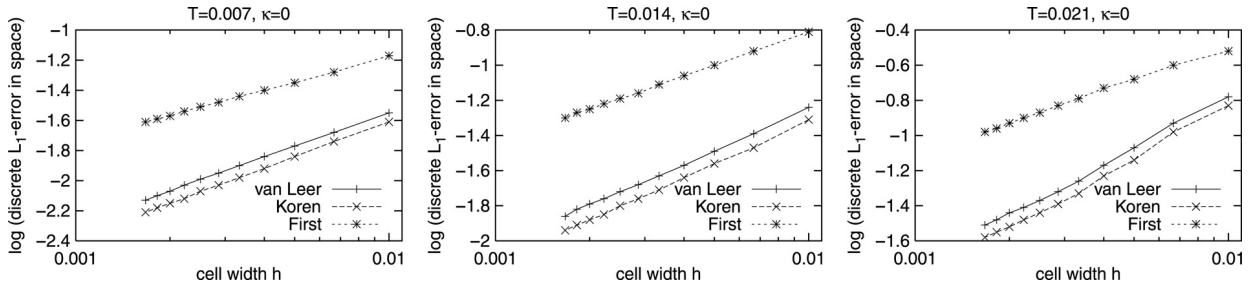


Fig. 5. The same as in Fig. 3 but with non-smooth initial data, $\varepsilon = 0$.

Table 2

Orders p and constants C ($\|\cdot\|_1$ -norm) corresponding to the plots of Fig. 5

	$T = 0.007$		$T = 0.014$		$T = 0.021$	
	C	p	C	p	C	p
Φ_{VL}	0.87	0.74	2.05	0.78	13.52	0.96
Φ_K	0.88	0.78	1.94	0.80	13.86	0.99
Φ_1	0.88	0.56	2.79	0.63	5.20	0.61

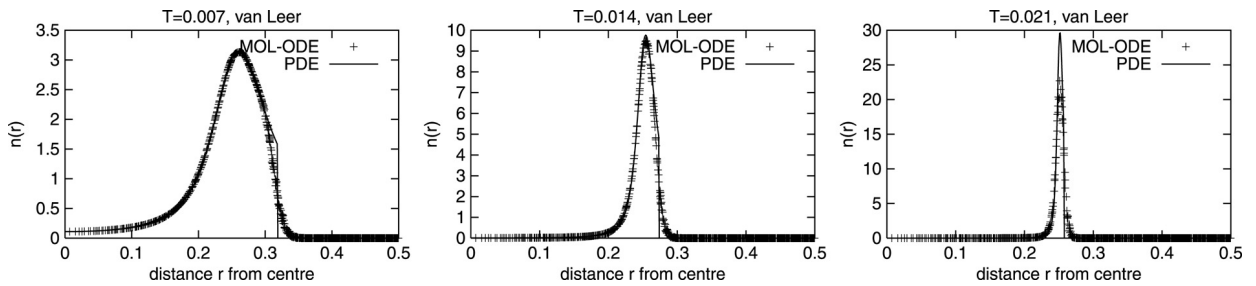


Fig. 6. The same as in Fig. 4 but with non-smooth initial data, $\varepsilon = 0$, and the van Leer limiter only.

[6, p. 121]. Also for non-smooth initial data we have nonnegativity of the solution and conservation of the initial mass up to machine precision. The plots in Fig. 6 show that the MOL-ODE solution is symmetric and they compare well with the results obtained for the same model in the paper by Tyson et al. [5]. We note that the computation times for the approximate non-smooth solutions with limiter Φ_K are considerably longer than with limiter Φ_{VL} .

To summarise, we discourage the application of first-order approximations of taxis terms because an excessive amount of grid points are necessary to obtain a spatial accuracy which is comparable to the accuracy obtained by using higher order discretizations on very coarse meshes already. Further, the Koren limiter gives generally more accurate approximations than the van Leer limiter. However, the differences are not very big and both limiters can be recommended for application.

4.2. Simulation of angiogenesis models

Model 1:

We consider the model of Chaplain and Stuart [2] (Eqs. (7) and (8)) in one space dimension, $\Omega = (0, 1)$. The initial conditions for the EC density and TAF concentration are given by

$$n(0, x_1) = \begin{cases} 1, & x_1 = 1, \\ 0, & \text{elsewhere} \end{cases}, \quad c_1(0, x_1) = \cos \frac{\pi x_1}{2}.$$

The boundary conditions imposed are

$$n(t, 1) = 1, \quad c_1(t, 1) = 0, \quad n(t, 0) = 0, \quad c_1(t, 0) = 1.$$

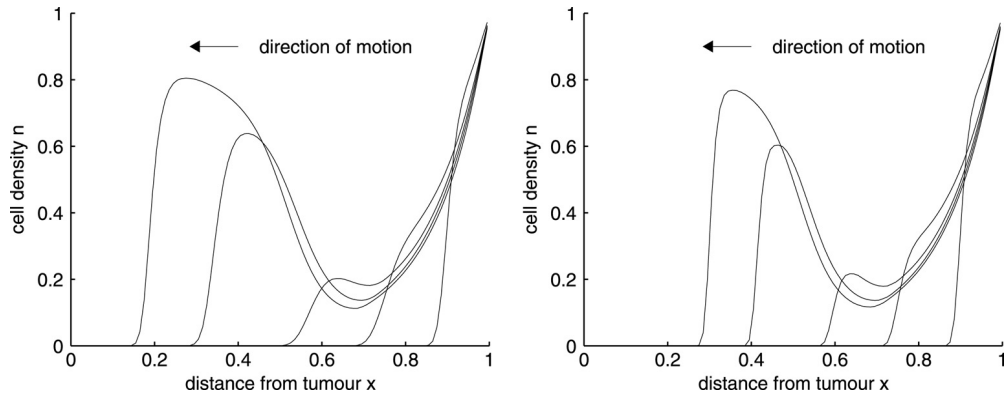


Fig. 7. Profile of the EC density at times $t = 0.1, 0.3, 0.5, 0.7, 0.8$ from a 1D simulation of Eq. (7), on the left, and (8), on the right. The parameter values are $\alpha = 10, \gamma = 1, \lambda = 1, \chi_0 = 0.75, \mu = 100, \beta = 4, c_1^* = 0.2$. In the left-hand figure the value of the cell random motility coefficient $\varepsilon = 0.001$, while in the right-hand figure this parameter is set to zero, i.e. $\varepsilon = 0$, no random motility.

The initial and boundary conditions assume a TAF source (tumour) at $x_1 = 0$ and a source of endothelial cells (parent blood vessel) at $x_1 = 1$. In the case of Eq. (8), no boundary condition can be prescribed for n at the outflow boundary $x_1 = 0$. The parameter values used in the simulation are given in Section 2.2.1.

Fig. 7 (left) shows the results from the simulation of Eq. (7) when $\varepsilon = 0.001$. As can be seen, the endothelial cell density moves out from the right-hand boundary. Initially there is little contribution from the proliferation term since the TAF concentration is below threshold. Around $t = 0.5$ proliferation begins to take place and the cell density profile evolves into a travelling wave-like structure. This is in qualitative agreement with experimental observations of angiogenesis.

Fig. 7 (right) shows the results from the simulation of (8), i.e. $\varepsilon = 0$. Qualitatively the results are similar. However, we note that the cell density profile moves from right to left more slowly in the absence of the diffusive term, i.e. the “wave speed” is slower in this case. By a time of $t = 0.8$ the advancing front in Fig. 7 (left) has almost reached $x = 0.1$, whereas in Fig. 7 (right) the front is only just beyond $x = 0.3$.

Model 2:

We now apply our scheme to the model of Anderson and Chaplain [11] (Eqs. (9) and (11)). The paper of Anderson and Chaplain [11] considered two different scenarios concerning the size and geometry of the tumour implant: a linear tumour source/implant and a circular tumour source/implant. Here we restrict ourselves to the case of a circular tumour implant and as a result model the initial (steady-state) TAF concentration profile as

$$c_1(0, x_1, x_2) = \begin{cases} 1, & 0 \leq r \leq 0.1, \\ \left(\frac{v-r}{v-0.1}\right)^2, & 0.1 \leq r \leq 1, \end{cases} \quad \text{where } v := \frac{\sqrt{5}-0.1}{\sqrt{5}-1},$$

and r is given by $r = ((x_1 - 1)^2 + (x_2 - 1/2)^2)^{1/2}$. This assumes that there is a circular tumour with a radius of 0.1 centred at $(1, 1/2)$. The value of v was chosen to ensure a decaying TAF concentration profile giving a value of $c_1 = 0.2$ at $r = 1$. Other functional forms for c_1 (giving a monotonic decay) can also be used. The initial fibronectin concentration is

$$c_2(0, x_1, x_2) = 0.75e^{-x_1^2/0.45}, \quad (x_1, x_2) \in [0, 1] \times [0, 1].$$

The initial conditions for the cells consisted of three discrete peaks of cells:

$$n(0, x_1, x_2) = \exp(-x_1^2/0.001) \max\{0, \sin(\pi(6x_2 - 1/2))\}^2.$$

The parameter values used in the simulations are given in Section 2.2.1.

Fig. 8 (top row) shows the cell density profile from the simulations of (9), $\varepsilon = 0.00035$, for times $t = 2, 5$ and 10. As can be seen, the initially unconnected clusters of cells move towards the circular tumour implant (TAF source) as well as moving laterally and connecting up with each other. This behaviour is qualitatively consistent with experimental observations for animal corneal models.

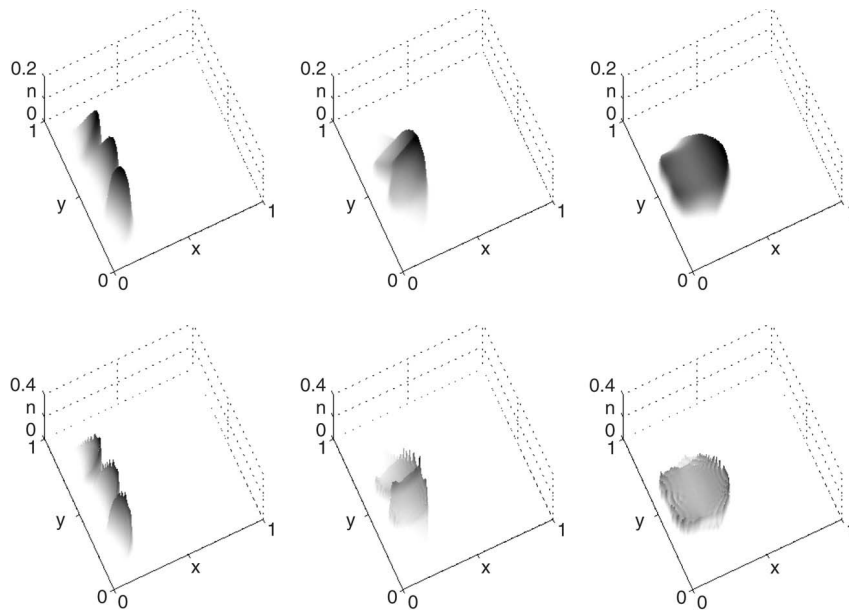


Fig. 8. Profiles of the endothelial cell density at times $t = 2, 5, 10$ from a 2D simulation of Eq. (9), top row, and (11), bottom row. The parameter values are $\chi_0 = 0.38, \rho_0 = 0.34, \alpha = 0.6, \beta = 0.05, \gamma = 0.1, \eta = 0.1$. The value of the cell random motility coefficient $\varepsilon = 0.00035$ in the top row plots, while in the bottom row plots this parameter is set to zero, i.e. $\varepsilon = 0$, no random motility.

Fig. 8 (bottom row) shows the cell density profile from the simulations of (11), i.e. the case $\varepsilon = 0$, for times $t = 2, 5$ and 10. Once again the solutions with and without cell random motility are qualitatively similar but the timescale is slower and the fronts are steeper/sharper in the case $\varepsilon = 0$.

4.3. Simulation of the invasion model

We now consider the tumour invasion model of Anderson et al. [18]. We will at first look at simulation results in one spatial dimension and then at simulations in two spatial dimensions with a heterogeneous initial concentration profile of the extracellular matrix.

4.3.1. Simulations in one dimension

In the one-dimensional case, initially we assume that there is a nodule of cells already present and that the tumour is centred around $x_1 = 0$ with n having the initial density distribution

$$n(0, x_1) = \begin{cases} \exp(-x_1^2/0.01), & x_1 \in [0, 0.25], \\ 0, & x_1 \in (0.25, 1]. \end{cases} \quad (36)$$

We assume that the tumour has already degraded some of its surrounding tissue and hence we take the initial profile of the ECM to be $c_1(0, x_1) = 1 - 0.5n(0, x_1)$. Finally, we assume that the initial MDE concentration profile is proportional to the initial tumour cell density and take $c_2(0, x_1) = 0.5n(0, x_1)$. The parameter values used are given in Section 2.2.2.

Fig. 9, top row, shows the results of the simulation of (12) in one dimension with $\varepsilon = 0.001$ at times $t = 1, 10, 20$. The results show the tumour cells degrading the tissue and then invading from left to right.

Fig. 9, bottom row, shows the results of the simulation of (15) in one dimension, i.e. $\varepsilon = 0$, at times $t = 1, 10, 20$. In this case we note that once again the tumour cells degrade the tissue and invade from left to right. However, in this case, the initial mass of tumour cells splits into two distinct clusters, with one cluster of tumour cells penetrating/invading deeply into the tissue. The other cluster of cells is left “stranded” behind at a position near $x = 0$. These cells cannot move anywhere since they have no random motion and there is no underlying ECM or ECM gradient since this has already been degraded to zero. We note that this result with $\varepsilon = 0$ is very similar to a result in Figure 2 of Anderson et al. [18] obtained by using nonlinear diffusion of the tumour cells.

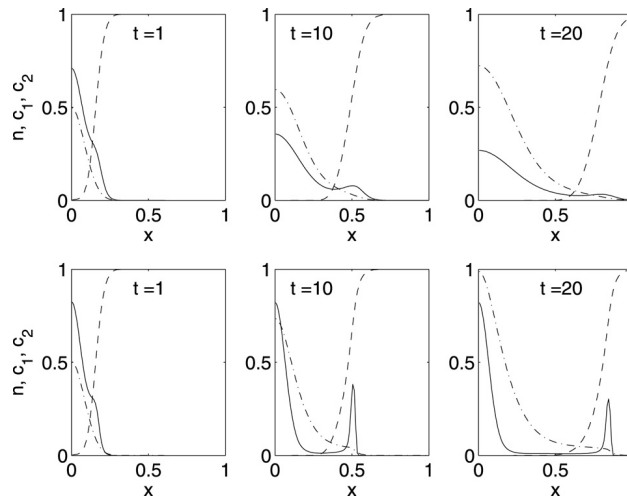


Fig. 9. Profiles of tumour cell density (—), ECM (---), and MDE (— · —) concentration at times $t = 1, 10, 20$ from a 1D simulation of Eq. (12), top row, and (15), bottom row. The parameter values are $d_2 = 0.001, \eta = 10, \chi = 0.005, \alpha = 0.1, \beta = 0$. The value of the cell random motility coefficient $\varepsilon = 0.001$ in the top row plots, while in the bottom row plots this parameter is set to zero, i.e. $\varepsilon = 0$, no random motility.

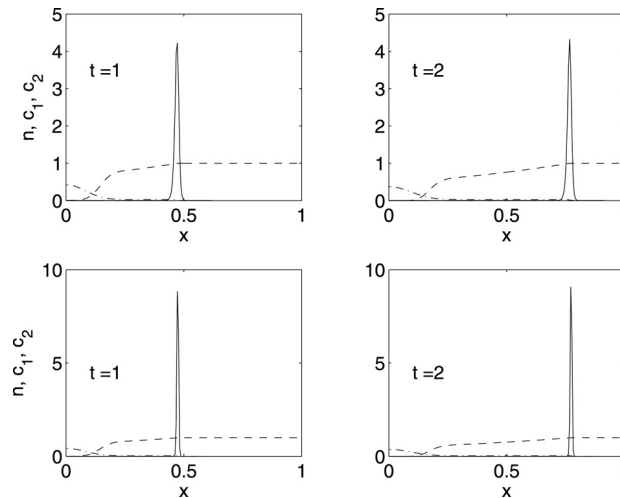


Fig. 10. Profiles of tumour cell density (—), ECM (---), and MDE (— · —) concentration at times $t = 1, 2$ from a 1D simulation (with $h = 1/200$) of Eq. (12), top row, and (15), bottom row. The haptotaxis coefficient χ is increased in these simulations and we use the parameter values $d_2 = 0.001, \eta = 10, \chi = 0.5, \alpha = 0.1, \beta = 0$. The value of the cell random motility coefficient $\varepsilon = 0.001$ in the top row plots, while in the bottom row plots this parameter is set to zero, i.e. $\varepsilon = 0$, no random motility.

Fig. 10, top row, shows the results of the simulation of (12) in one dimension with the change to parameter values of $\chi = 0.5$. With the increased haptotaxis coefficient, this dominates random motion and we see the evolution of a single separate wave of invading tumour cells. This is reminiscent of a highly aggressive cancer. Fig. 10, bottom row, shows the results of the simulation of (15) in one dimension with $\chi = 0.5$. In this situation the numerical solution is qualitatively similar to the plots in the top row. There is some difference in the height of the wave and in the wave speed. As is to be expected, in the case of zero random motility (bottom row), the wave is slightly slower.

4.3.2. Simulations with heterogeneous ECM density in 2D

We now consider tumour invasion in two spatial dimensions. This enables us to consider the effect of spatial heterogeneity explicitly. In particular we can consider a heterogeneous ECM which is more representative of real tissue. To this end a hypothetical heterogeneous initial ECM density c_1 is used as depicted in Fig. 11. There are regions of higher and lower density which should lead to a different dynamic of the cell movement compared to the

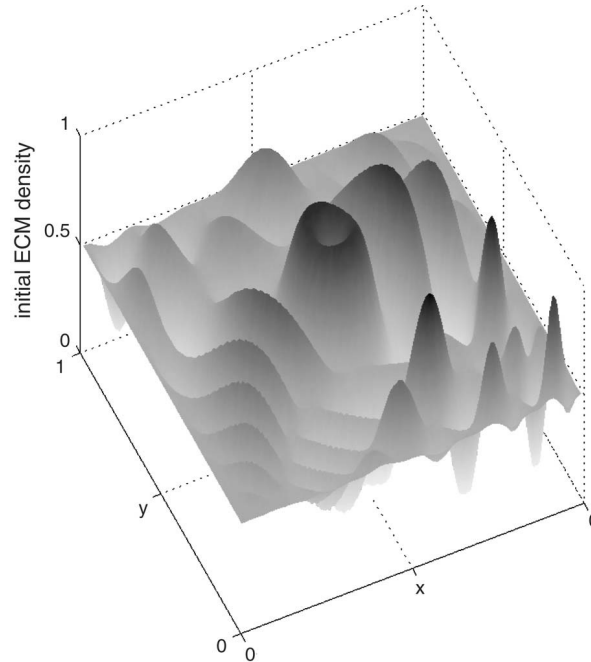


Fig. 11. Heterogeneous initial ECM density $c_1(0, x_1, x_2)$.

1D simulations. The initial condition for tumour cell density n and MDE concentration c_2 are chosen as

$$n(0, x_1, x_2) = \begin{cases} \exp(-r^2/0.0025), & r \in [0, 0.1] \\ 0, & r \in (0.1, 1], \end{cases}$$

$$c_2(0, x_1, x_2) = 0.5n(0, x_1, x_2), \quad r^2 = (x_1 - 0.5)^2 + (x_2 - 0.5)^2.$$

The parameter values used are given in [Section 2.2.2](#).

[Fig. 12](#) shows the cell density profile at times $t = 1, 4, 7, 15$ from the simulation of [Eq. \(12\)](#) with $\varepsilon = 0.001$. The tumour cell density invades the tissue (as expected) but the underlying spatial heterogeneity causes the tumour cell density to “break up” and fragment.

[Fig. 13](#) shows the cell density profile at times $t = 1, 4, 7, 15$ from the simulation of [Eq. \(15\)](#) i.e. $\varepsilon = 0$. In this case we see a quantitative difference between the two solutions. Once again the tumour cells invade the tissue and the underlying heterogeneity causes the tumour cell density to “break up”. However, in this case the maximum value of the cell density varies by one order of magnitude (around 0.5 in the case $\varepsilon = 0$ compared to around 0.05 in the case $\varepsilon = 0.001$). Diffusion has caused the cell density to spread out “more thinly” in the domain. Also, we note that in the zero-diffusion case, the cell density profile develops steeper transition fronts. The simulation with zero random motility shows the same qualitative behaviour as the solution with random motility. However, the moving tumour cell fronts are much more sharply defined and more compact which in turn leads to higher peak densities in the zero-random-motility case.

The initial cell mass is approximately conserved throughout the simulation with a maximum error of about 10^{-14} .

4.4. Simulation of Dd aggregation

We now consider the model of Höfer [31] for aggregation in *D. discoideum* (Dd), [Eqs. \(16\)](#) and [\(17\)](#). Here we present simulation results for Dd aggregation in 2D. The initial conditions used for the Dd cells, the receptors and the cAMP are shown in [Fig. 14](#). The parameter values used are given in [Section 2.3](#).

[Fig. 15](#) shows the results at times $t = 10, 20, 40$ for the simulations of [\(16\)](#) with $\varepsilon = 0.012$. These show the cells aggregating towards the centre of the spiral and the formation of streams with the break-up of the spirals.

[Fig. 16](#) shows the results at times $t = 10, 20, 40$ for the simulations of [\(17\)](#), i.e. $\varepsilon = 0$. Once again the results are qualitatively similar. The cells aggregate towards the centre of the spiral and they form streams which break up of the

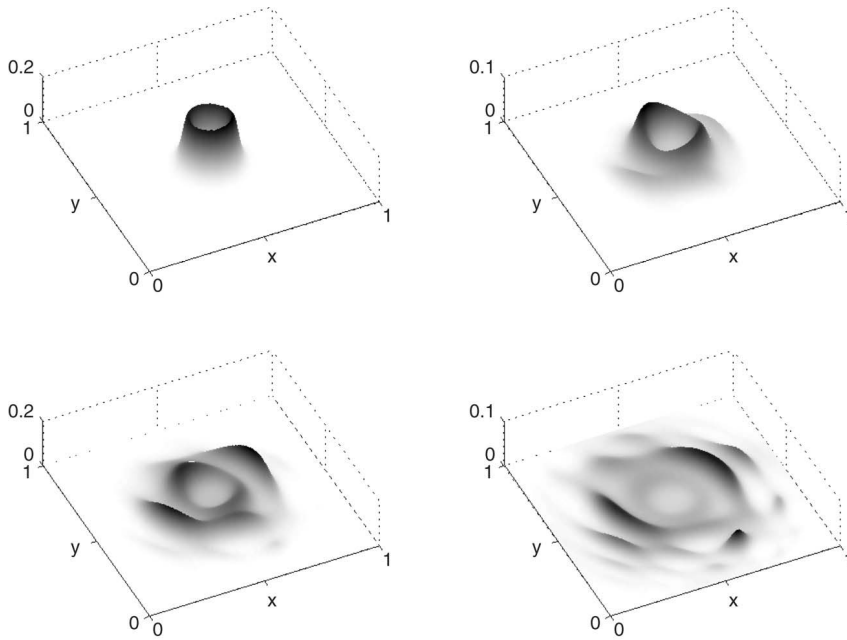


Fig. 12. Profiles of the tumour cell density at times $t = 1, 4, 7, 15$ from a 2D simulation of Eq. (12). The parameter values are $\varepsilon = 0.001, d_2 = 0.001, \eta = 10, \chi = 0.005, \alpha = 0.1, \beta = 0.5$, so a decay of the MDE is included in the simulation.

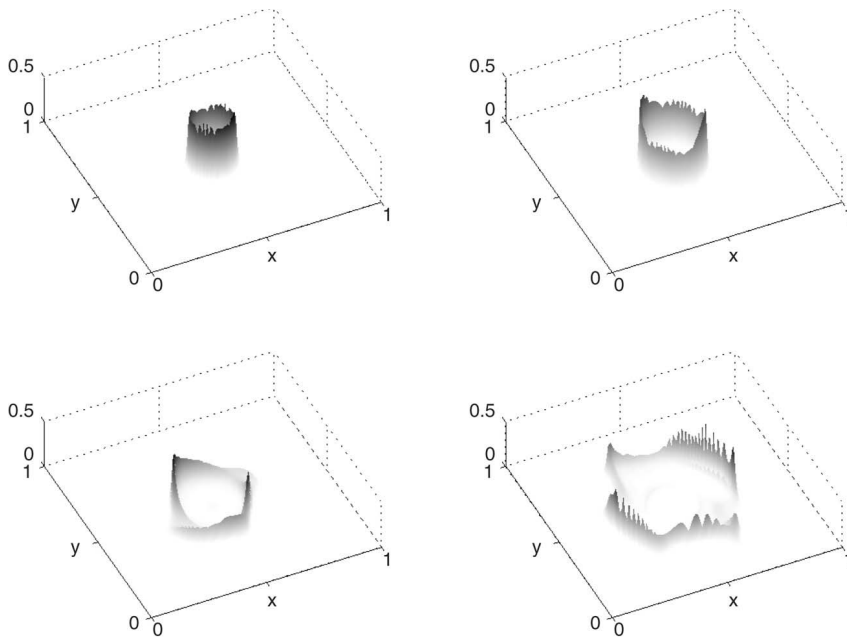


Fig. 13. Profiles of the tumour cell density at times $t = 1, 4, 7, 15$ from a 2D simulation of Eq. (15). The parameter values are $\varepsilon = 0, d_2 = 0.001, \eta = 10, \chi = 0.005, \alpha = 0.1, \beta = 0.5$.

spirals. We see that there have developed two separated clusters of cells in the case of no cell random motility. This does not occur for all initial cell densities but it does for some.

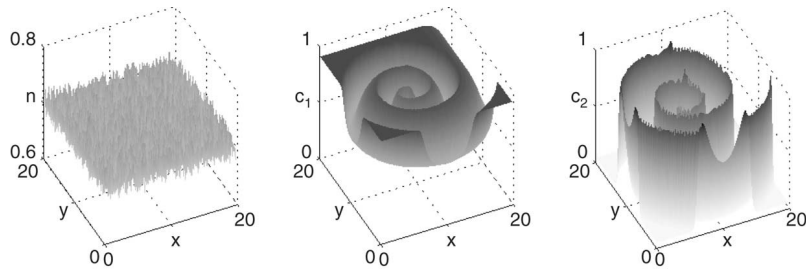


Fig. 14. Initial conditions for the Dd model simulation: Dd density (n , left), active receptors (c_1 , middle), and cAMP concentration (c_2 , right).

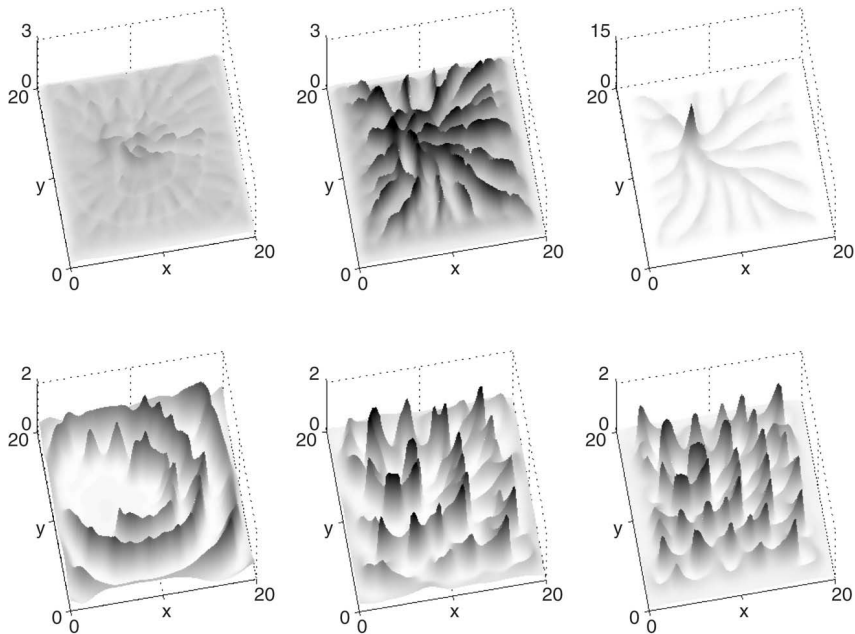


Fig. 15. Dd density (top row) and cAMP concentration (bottom row) profiles for the Dd aggregation model (16) at times $t = 10, 20, 40$ (left to right). The parameter values used are as given in Section 2.3.

5. Discussion and conclusion

In this paper we have studied multi-dimensional taxis–diffusion–reaction systems and presented novel, efficient, robust numerical techniques for the computation of solutions of these models. The systems we have studied are characterised by having one equation containing nonlinear advection terms (taxis) which are large in magnitude when compared with the random motility terms. These systems are difficult to treat numerically (particularly in the absence of any random motility term).

Our numerical scheme is based on the method of lines. The spatial derivatives are approximated by following the finite volume approach and this naturally respects the conservation of mass property of the underlying conservation laws. Special attention is paid to the discretization of the nonlinear advection/taxis terms. Here we use limiter functions in order to avoid non-physical oscillations in the solution and this in turn prevents negative solution values. As a result of the discretization in space we obtain a system of ordinary differential equations (MOL-ODE) which only admits nonnegative solutions (for nonnegative initial data). Having this property guaranteed is especially valuable because negative solution values could turn stable reactions in the model into unstable ones and this is of course highly undesirable. In the second step of the method of lines we solve the MOL-ODE by using splitting techniques employing explicit Runge–Kutta and Runge–Kutta–Rosenbrock methods. Splitting is applied for two reasons. Firstly, systems containing the nonlinear advection term only are more efficiently solved by explicit methods (e.g. the RK32

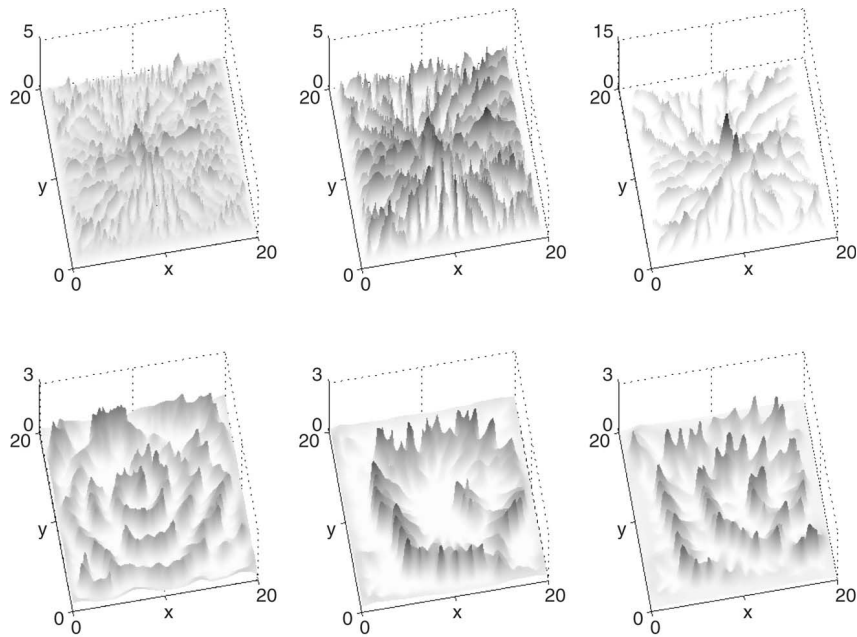


Fig. 16. Dd density (top row) and cAMP concentration (bottom row) profiles for the Dd aggregation model (17) at times $t = 10, 20, 40$ (left to right). The parameter values used are as given in Section 2.3.

method considered here) whereas systems containing diffusion and reaction only require an implicit treatment because of stiffness. Secondly, splitting is employed to significantly reduce the linear algebra costs in the (linearly) implicit time stepping scheme (this is not important in 1D simulations of the models but already essential in 2D). Judging by the numerical results (see also [7,40]), we can recommend the methods described, OPS-RK32 and AMF-RK32, for the solution of the MOL-ODE.

Recently Tyson et al. [5] have described a splitting algorithm and applied it to a specific TDR model. They perform a splitting of the TDR model already at the PDE level and their approach is closely related to our proposed OPS schemes. They use the software package CLAWPACK [48] to deal with the taxis part of the problem and also an L -stable implicit method for the diffusion–reaction part. The AMF methods presented here differ from these two approaches as they do not split the equations and hence avoid the associated splitting error.

In addition to the numerical aspect of the paper, there are also implications for modelling biological systems involving the migration of certain species in response to external stimuli. Many models in the literature always assume that all species have a random motility component to their movement and that this can be modelled using classical Fickian diffusion. However, as is well known (cf. the fundamental solution to the heat equation) this poses certain problems in terms of speed of propagation and distribution of compact support initial data.

Consider the simplest scalar equation composed of a “linear” random motion term, a “linear” advection term and the simplest, realistic proliferation term (logistic growth):

$$\partial_t n = \varepsilon \Delta n - \kappa \partial_x n + \mu n(1 - n).$$

Intuitively, with a Cauchy problem (pure initial value problem, infinite domain) we can think of the three components (random motility, advection and proliferation) acting in the following ways:

- random motion spreads the initial data out;
- the advection term moves the initial data with speed κ ;
- the proliferation term drives the initial data to the steady state of 1 at rate μ .

If we look for travelling wave solutions to the above equation we find that the minimum wave speed is $\kappa + \sqrt{2\varepsilon\mu}$. By setting either of the parameters ε or κ to zero we obtain a slower wave. From the computational experiments we have carried out in this paper we see that this is the case, i.e. a faster wave speed is observed in the cases where ε does not equal zero; cf. Figs. 7–10, 12 and 13.

Of course other more realistic modelling approaches are possible; for example one can consider nonlinear diffusion, e.g.

$$\partial_t n = \nabla \cdot (\varepsilon(n) \nabla n) - \kappa \partial_x n + \mu n(1 - n)$$

or one could consider reaction–telegraph models of the form [49]:

$$\partial_t n = -\partial_{tt} n + \varepsilon \Delta n + f(n) + \partial_t(f(n)).$$

There is therefore a need to properly model the migration of species from the outset. Not all systems necessarily have random motion terms and there is good reason not to include random motion in certain model systems. Indeed this has recently been receiving some overdue attention in the literature [50–53]. It is probably more realistic to either include some kind of nonlinear random motion [54], or, where appropriate, not to include random motion at all. However, this complicates the numerical analysis (see paragraph 1). A balance must be achieved between realistic modelling and complexity of simulation. An important consideration is the extent to which model results are qualitative or quantitative. Nonetheless, even in systems where the random motility component is small in magnitude compared to the taxis component, appropriate and accurate numerical schemes, such as those in this paper, should be used.

References

- [1] J.D. Murray, *Mathematical Biology*, 2nd edition, Springer-Verlag, Berlin, 1993.
- [2] M.A.J. Chaplain, A.M. Stuart, A model mechanism for the chemotactic response of endothelial cells to tumour angiogenesis factor, *IMA J. Math. Appl. Med. Biol.* 10 (1993) 149–168.
- [3] G.P. Boswell, H. Jacobs, F.A. Davidson, G.M. Gadd, K. Ritz, A positive numerical scheme for a mixed-type partial differential equation model for fungal growth, *Appl. Math. Comput.* 138 (2003) 321–340.
- [4] A. Bailón-Plaza, M.C.H. van der Meulen, A mathematical framework to study the effects of growth factor influences on fracture healing, *J. Theor. Biol.* 212 (2001) 191–209.
- [5] R. Tyson, L.G. Stern, R.J. LeVeque, Fractional step methods applied to a chemotaxis model, *J. Math. Biol.* 41 (2000) 455–475.
- [6] R.J. LeVeque, *Numerical Methods for Conservation Laws*, 2nd edition, in: *Lectures in Mathematics*, Birkhäuser, 1992.
- [7] A. Gerisch, *Numerical methods for the simulation of taxis–diffusion–reaction systems*, Ph.D. Thesis, Martin-Luther Universität Halle-Wittenberg, 2001.
- [8] D.W. Thompson, *On Growth and Form*, Cambridge University Press, 1917.
- [9] D. Balding, D.L.S. McElwain, A mathematical model of tumour-induced capillary growth, *J. Theor. Biol.* 114 (1985) 53–73.
- [10] M.E. Orme, M.A.J. Chaplain, A mathematical model of the first steps of tumour-related angiogenesis: Capillary sprout formation and secondary branching, *IMA J. Math. Appl. Med. Biol.* 13 (1996) 73–98.
- [11] A.R.A. Anderson, M.A.J. Chaplain, Continuous and discrete mathematical models of tumor-induced angiogenesis, *Bull. Math. Biol.* 60 (1998) 857–899.
- [12] H.A. Levine, B.D. Sleeman, M. Nilsen-Hamilton, Mathematical modeling of the onset of capillary formation initiating angiogenesis, *J. Math. Biol.* 42 (2001) 195–238.
- [13] S.R. McDougall, A.R.A. Anderson, M.A.J. Chaplain, J.A. Sherratt, Mathematical modelling of flow through vascular networks: Implications for tumour-induced angiogenesis and chemotherapy strategies, *Bull. Math. Biol.* 64 (2002) 673–702.
- [14] A. Stephanou, S.R. McDougall, A.R.A. Anderson, M.A.J. Chaplain, Mathematical modelling of flow in 2d and 3d vascular networks: Applications to anti-angiogenic and chemotherapeutic drug strategies, *Math. Comput. Modelling* 41 (2005) 1137–1156.
- [15] J. Valenciano, M.A.J. Chaplain, Computing highly accurate solutions of a tumour angiogenesis model, *Math. Models Methods Appl. Sci.* 13 (2003) 747–766.
- [16] J. Valenciano, M.A.J. Chaplain, An explicit subparametric spectral element method of lines applied to a tumour angiogenesis system of partial differential equations, *Math. Models Methods Appl. Sci.* 14 (2004) 165–187.
- [17] R.O. Hynes, *Fibronectins*, Springer-Verlag, New York, 1990.
- [18] A.R.A. Anderson, M.A.J. Chaplain, E.L. Newman, R.J.C. Steele, A.M. Thompson, Mathematical modelling of tumour invasion and metastasis, *J. Theor. Med.* 2 (2000) 129–154.
- [19] A.J. Perumpanani, J. Norbury, J.A. Sherratt, H.M. Byrne, Biological inferences from a mathematical model for malignant invasion, *Invasion Metastasis* 16 (1996) 209–221.
- [20] R.A. Gatenby, E.T. Gawlinski, A reaction–diffusion model of cancer invasion, *Cancer Res.* 56 (1996) 5745–5753.
- [21] B.P. Marchant, J. Norbury, A.J. Perumpanani, Traveling shock waves arising in a model of malignant invasion, *SIAM J. Appl. Math.* 60 (1999) 463–476.
- [22] C.J. Weijer, The role of chemotactic cell movement in *Dictyostelium* morphogenesis, in: M.A.J. Chaplain, G.D. Singh, J.C. McLachlan (Eds.), *On Growth and Form: Spatio-temporal Pattern Formation in Biology*, in: *Wiley Series in Mathematical and Computational Biology*, John Wiley & Sons Ltd., Chichester, 1999, pp. 173–199.
- [23] E. Keller, L. Segel, Initiation of slime mold aggregation viewed as instability, *J. Theor. Biol.* 26 (1970) 399–415.

- [24] T. Höfer, J.A. Sherratt, P.K. Maini, Cellular pattern formation during Dictyostelium aggregation, *Physica D* 85 (1995) 425–444.
- [25] B.N. Vasiev, P. Hogeweg, A.V. Panfilov, Simulation of Dictyostelium discoideum aggregation via reaction–diffusion model, *Phys. Rev. Lett.* 73 (1994) 3173–3176.
- [26] A.A. Polezhaev, V.S. Zykov, S.C. Müller, Destabilization of cell aggregation under nonstationary conditions, *Phys. Rev. E* 58 (1998) 6328–6332.
- [27] C. van Oss, A.V. Panfilov, P. Hogeweg, C.J. Weijer, Spatial pattern formation during aggregation of the slime mould Dictyostelium discoideum, *J. Theor. Biol.* 181 (1996) 203–213.
- [28] B.N. Vasiev, C.J. Weijer, Modelling chemotactic cell sorting during Dictyostelium discoideum mound formation, *Biophys. J.* 76 (1999) 595–605.
- [29] J.C. Dallon, H.G. Othmer, A discrete cell model with adaptive signaling for aggregation of Dictyostelium discoideum, *Philos. Trans. R. Soc. Lond. B* 352 (1997) 391–417.
- [30] A.W. Pitcairn, Mathematical modelling of the aggregation behaviour of Dictyostelium discoideum, Ph.D. Thesis, University of Dundee, 2003.
- [31] T. Höfer, Modelling Dictyostelium aggregation, Ph.D. Thesis, University of Oxford, 1996.
- [32] W. Hundsdorfer, J.G. Verwer, Numerical Solution of Time-Dependent Advection–Diffusion–Reaction Equations, in: Springer Series in Computational Mathematics, vol. 33, Springer-Verlag, Berlin, Heidelberg, New York, 2003.
- [33] N. Bellomo, L. Preziosi, Modelling Mathematical Methods and Scientific Computation, in: CRC Mathematical Modelling Series, CRC Press, 1995.
- [34] W. Hundsdorfer, B. Koren, M. van Loon, J.G. Verwer, A positive finite-difference advection scheme, *J. Comput. Phys.* 117 (1) (1995) 35–46.
- [35] A. Gerisch, D.F. Griffiths, R. Weiner, M.A.J. Chaplain, A positive splitting method for mixed hyperbolic–parabolic systems, *Numer. Methods Partial Differential Equations* 17 (2001) 152–168.
- [36] A. Gerisch, Finite difference methods for coupled nonlinear hyperbolic and parabolic partial differential equations in one and two dimensions, Master’s Thesis, University of Dundee, 1997.
- [37] P.K. Sweby, High resolution schemes using flux limiters for hyperbolic conservation laws, *SIAM J. Numer. Anal.* 21 (1984) 995–1011.
- [38] B. Koren, A robust upwind discretization method for advection, diffusion and source terms, in: C.B. Vreugdenhill, B. Koren (Eds.), *Numerical Methods for Advection–Diffusion Problems*, in: Notes on Numerical Fluid Mechanics, vol. 45, Vieweg, Braunschweig, 1993, pp. 117–138 (Chapter 5).
- [39] Z. Horváth, Positivity of Runge–Kutta and diagonally split Runge–Kutta methods, *Appl. Numer. Math.* 28 (2–4) (1998) 309–326.
- [40] A. Gerisch, J. Verwer, Operator splitting and approximate matrix factorization for taxis–diffusion–reaction models, *Appl. Numer. Math.* 42 (2002) 159–176.
- [41] A. Gerisch, R. Weiner, The positivity of low order explicit Runge–Kutta schemes applied in splitting methods, *Comput. Math. Appl.* 45 (2003) 53–67.
- [42] B. Gustafsson, H.-O. Kreiss, J. Olinger, *Time Dependent Problems and Difference Methods*, John Wiley & Sons, Inc., 1995.
- [43] J.G. Verwer, W.H. Hundsdorfer, J.G. Blom, Numerical time integration for air pollution models, Report MAS-R9825, CWI, 1998.
- [44] J.G. Verwer, E.J. Spee, J.G. Blom, W. Hundsdorfer, A second-order Rosenbrock method applied to photochemical dispersion problems, *SIAM J. Sci. Comput.* 20 (4) (1999) 1456–1480.
- [45] P.J. van der Houwen, B.P. Sommeijer, Approximate factorization for time-dependent partial differential equations, Report MAS-R9915, CWI, 1999.
- [46] G. Strang, On the construction and comparison of difference schemes, *SIAM J. Numer. Anal.* 5 (1968) 506–517.
- [47] E. Hairer, S.P. Nørsett, G. Wanner, *Solving Ordinary Differential Equations. I. Nonstiff Problems*, 2nd edition, in: Springer Series in Computational Mathematics, vol. 8, Springer-Verlag, Berlin, 1993.
- [48] R.J. LeVeque, *CLAWPACK User Guide and Software*, Available from <http://www.amath.washington.edu/~claw>.
- [49] E.E. Holmes, Are diffusion models too simple? A comparison with telegraph models of invasion, *Amer. Naturalist* 142 (1993) 779–795.
- [50] S. Dunbar, A branching random walk evolution and a nonlinear hyperbolic equation, *SIAM J. Appl. Math.* 48 (1988) 1510–1526.
- [51] K.P. Hadeler, Travelling fronts in random walk systems, *Forma* 10 (1995) 223–233.
- [52] K.P. Hadeler, Travelling fronts for correlated random walks, *Can. Appl. Math. Q.* 2 (1994) 27–43.
- [53] K.P. Hadeler, Hyperbolic travelling fronts, *Proc. Edinb. Math. Soc.* 31 (1988) 89–97.
- [54] K. Lika, T.G. Hallam, Traveling wave solutions of a nonlinear reaction–advection equation, *J. Math. Biol.* 38 (1999) 346–358.